Analytical Models for the Thrust of a Rotating Detonation Engine

Joseph E. Shepherd
Professor of Aeronautics and Mechanical Engineering
joseph.e.shepherd@caltech.edu
Graduate Aerospace Laboratories
California Institute of Technology
Pasadena, CA 91125 USA

Jiro Kasahara
Professor of Aerospace Engineering
kasahara@nuae.nagoya-u.ac.jp
Nagoya University
Nagoya, Aichi, 464-8603, JAPAN

GALCIT Report FM2017.001
Graduate Aerospace Laboratories
California Institute of Technology
Pasadena CA 911125 USA

September 23, 2017

Abstract

Two models are proposed for rotating detonation engine performance. The first model is motivated by models of pulse detonation engine performance which are based on the pressure-time history within the detonation tube. The present work extends those ideas to treat rotating detonation engines with a control volume analysis that considers the forces within the combustion chamber. The key scaling parameters for this model are the height of the reactant layer just ahead of the detonation wave and the computed Chapman-Jouguet pressure and velocity. The thrust can be estimated using these parameters and a simple functional form of the pressure history on the injector surface. The second model is based on the approximation of mean axial flow and uses a conventional control volume analysis that focuses on exit conditions to evaluate thrust. The axial flow speed and thrust are evaluated based on approximating the flow following the detonation as isentropic and considering a two-dimensional expansion that converts azimuthal motion into purely axial flow. Numerical and analytic evaluation of these models demonstrates that predicted thrust and specific impulse exhibit the same scaling relationships with mixture properties as pulse detonation engines.

Contents

List of Figures

List of Tables

1 Introduction

The *rotating detonation engine* or RDE (Fig. 1a) is based on continuous flow through an annular chamber in which combustion takes place through a transversely rotating detonation. The fuel and oxidizer are injected at the entrance of the combustor and the high-pressure combustion products behind the detonation wave expand and turn to create a primarily axial flow at the exit of the combustion chamber. The reviews by Rankin et al. (2017) and Zhou et al. (2016) provide more details about RDEs and Kailasanath (2017) summarizes recent studies. Although variants of the combustor shown in Fig. 1a are being considered as components in air-breathing propulsion systems, in the present study we examine the performance of the annular combustor in a rocket motor configuration.[1] For actual rocket motor applications, an obvious extension is to add an exhaust nozzle; this is not the focus of the present study although the effect of an ideal nozzle is briefly considered.

The purpose of the present article is to provide two simple analytical methodologies for computing the thrust of the configuration of Fig. 1a. The first methodology, termed the "pressure history model", is motivated by the success of ideas that were originally developed for pulse detonation engines (PDE) (Wintenberger et al., 2003; Endo et al., 2004) and the observations (Rankin et al., 2017; Fotia et al., 2017) that models developed to predict PDE performance appear to be quantitatively useful for RDEs. We shall demonstrate that although the principles of operation appear to be quite different for RDE and PDE operation, it is possible to use very similar modeling ideas to predict RDE performance under certain conditions. The second methodology, termed the "axial flow model", is based on the approximation of mean axial flow and uses a conventional control volume analysis that focuses on exit conditions to evaluate thrust. This model is motivated by the results of numerical simulations that show the approach to axial flow with downstream distance and the success of Kato et al. (2016) in using conventional rocket motor performance analyses in correlating RDE test results. The axial flow speed and thrust are evaluated by approximating the flow following the detonation as isentropic and considering a two-dimensional expansion that converts azimuthal motion into purely axial flow.

In order to make progress with analytical modeling, we will need to make a number of simplifying assumptions. First, we will assume that the fuel and oxidizer are supplied at a constant average rate, are well mixed and the detonation wave moves at a constant speed U_D. Under these conditions, we can further assume that the flow within the engine will be periodic in time. Viewed from the laboratory frame, as shown in Fig. 1a, the detonation wave appears to rotate with angular speed $\omega = U_D/\overline{R}$ in the azimuthal direction, which gives the device its name. The actual detonation speed, U_D in Fig. 1a, may differ from the Chapman-Jouguet (CJ) speed for a number of reasons such as incompletely mixed fuel and oxidizer, the influence of the expanding flow within the reaction zone immediately behind the wave and the upstream velocity of the unburned gas. In our models, we will assume that the detonation propagates with the CJ speed relative to the incoming flow.

Second, we assume that there is a single detonation front within the chamber and the flow will oscillate with frequency $f = \omega/2\pi$. The flow properties will be periodic with temporal period $T = 1/f$. This greatly simplifies the analysis because in a frame co-rotating with the detonation, the flow will be steady. This corresponds to transforming to a coordinate $\theta' = \theta - \omega t$ and eliminating

[1] Due to the large total pressure loss associated with the arrays of small slots or holes used to inject the fuel and oxidizer, there are a number of challenges in incorporating these combustion chambers into the core of a gas turbine or similar high-mass-flow engine.

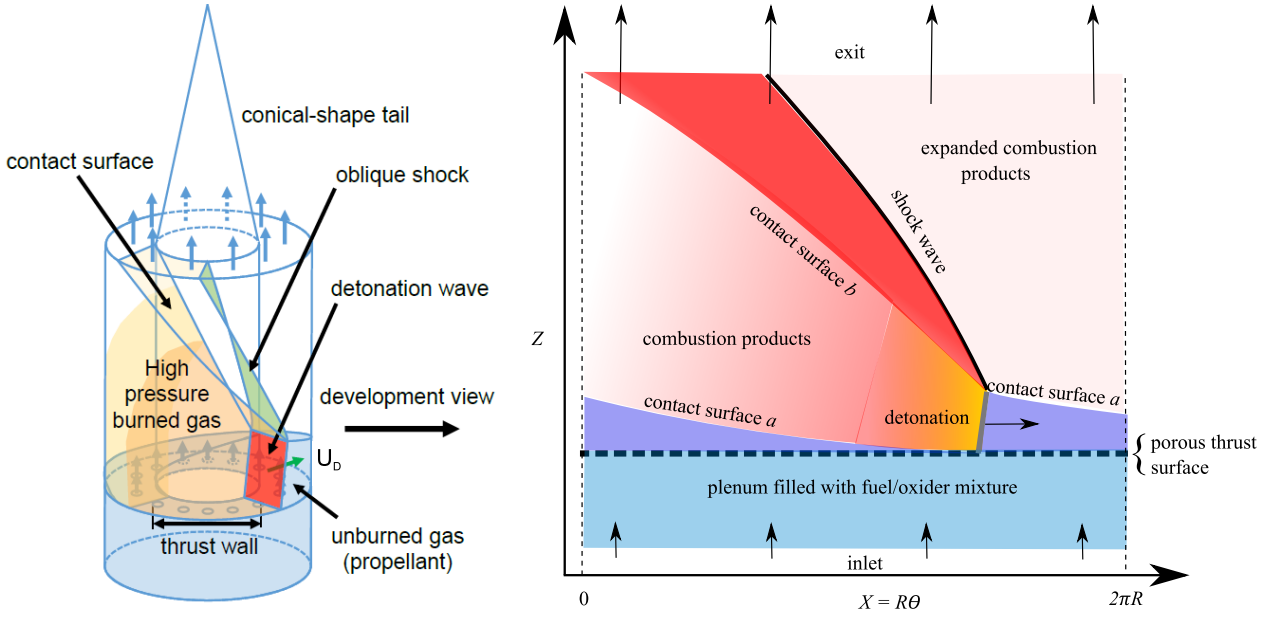

Figure 1: a) A rotating detonation engine test fixture (Ishihara et al., 2015). b) Schematic of "unwrapped" flow field projected onto the θ - Z plane.

time as a variable. For example, the pressure can be written as $P = P(r, \theta, z, t) = P(r, \theta - \omega t, z) = P(r, \theta', z)$. The restriction to a single wave turns out to be artificial and we will show that the results for one wave can be easily extended to multiple waves.

Third, we will assume that radial variations in the flow can be neglected and the flow can be approximated as two-dimensional in space, i.e., $P(\theta', z)$. Developing ("unwrapping") the surface of the cylinder onto a plane and considering the flow to be uniform in the radial direction reduces the geometry to the X-Z plane with the flow field shown in schematic of Fig. 1b. In the X-Z plane, the flow is spatially periodic in the X direction, $f(x + 2\pi\overline{R}, z) = f(x, z)$ with period $2\pi\overline{R}$. This representation is commonly employed in many numerical simulations of RDEs. Eude et al. (2011) have compared pressure distributions computed from two and three-dimensional simulations and demonstrated that integral (average) properties are insensitive to three-dimensional effects and two-dimensional models are adequate for predicting properties such as thrust. The transformation to a two-dimensional system that is co-rotating with the detonation wave is presented in Appendix A

By averaging over a period, the azimuthal and time dependence of the flow can be eliminated from consideration to facilitate the computation of average thrust. For the purposes of developing simple models, the variations in the radial direction are also averaged so that the flow in the combustion chamber can be considered quasi-one dimensional with average properties dependent only on the axial distance z. For example, the pressure can be averaged to obtain

$$\overline{P}(z) = \frac{1}{T}\int_t^{t+T} \frac{1}{2\pi\overline{R}W}\int_{R_i}^{R_o} P(r,\theta,z,t)\, 2\pi r \,\mathrm{d}r\,\mathrm{d}t = \frac{1}{2\pi}\int_0^{2\pi}\frac{1}{\overline{R}W}\int_{R_i}^{R_o} P(r,\theta',z)\, r\,\mathrm{d}r\,\mathrm{d}\theta' \,, \quad (1)$$

where $W = R_o - R_i$ is the radial width of the combustion chamber, assumed to be constant for the purposes of analysis and $\overline{R} = (R_o + R_i)/2$ is the mean radius of the combustion chamber annulus.

In the co-rotating reference frame, the time averaging is equivalent to averaging over the azimuthal angle θ, as shown in the second version of the integral in (1).

2 Control Volume Analysis of Thrust

The thrust for an engine without an exit nozzle, i.e., just a straight combustion chamber, can be evaluated using the standard approach of evaluating the integral momentum balance over a control volume surface A surrounding the engine,

$$\int_A \rho \boldsymbol{u}\boldsymbol{u} \cdot \boldsymbol{n}\, \mathrm{d}S + \int_A P\boldsymbol{n}\, \mathrm{d}S = \int_A \boldsymbol{\tau} \cdot \boldsymbol{n}\, \mathrm{d}S + \boldsymbol{F} \ . \tag{2}$$

Two possible control volumes are shown in Fig 2. These control volumes and the idealized combustion chamber are axially symmetric. The force $\boldsymbol{F}$ is the reaction force needed to keep the engine stationary; it is equal in magnitude and opposite in direction to the thrust. For both control volumes, we assume that the pressure on the exterior of the engine is everywhere equal to the atmospheric pressure P_a. These control volumes and the simplifying assumptions are identical to those used in the PDE models of Wintenberger et al. (2003) and Endo et al. (2004).

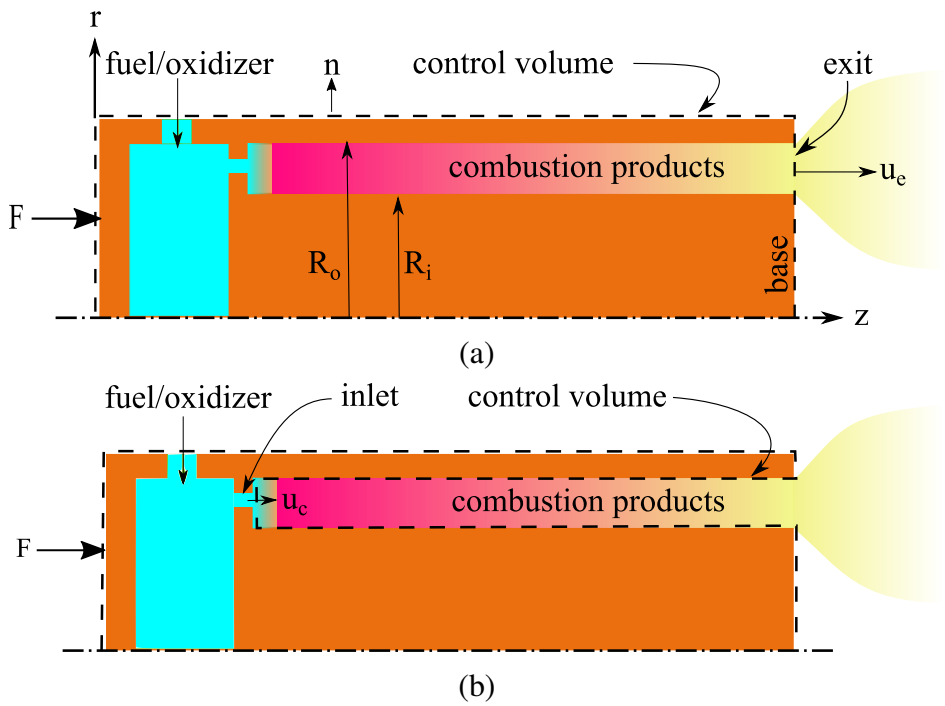

Figure 2: Two approaches to formulating a control volume for a rotating detonation engine to compute thrust base on a) chamber exit conditions. b) combustion chamber inlet conditions.

The control volume of Fig. 2a completely encloses the entire engine and crosses the exit plane of the combustor. This enables the computation of the thrust based on exit conditions. The balance of forces in the axial (z) direction for this control volume, assuming static conditions and uniform

pressure everywhere except at the exit, is:

$$F_z = \int_{A_e} \rho_e u_{z,e}^2 \, \mathrm{d}S + \int_{A_e} (P_e - P_a) \, \mathrm{d}S \; . \tag{3}$$

To evaluate the integrals, we apply the averaging method described in the introduction to compute the average magnitude of the thrust $\mathcal{T} = \overline{F}_z$. The momentum of the fuel/oxidizer supply does not contribute to the force balance because the supply is assumed to enter perpendicular to the axial direction. In order to use this version of the thrust computation, the entire flow field within the combustor must be analyzed in order to define the exit conditions. This is the approach taken by many previous researchers Fievisohn and Yu (2017); Schwer and Kailasanath (2013, 2011b). If the flow at the exit of the combustor is uniform, then the thrust expression is the same as that used in idealized rocket motor models

$$\mathcal{T} = \dot{M}\overline{u_e} + A_e(\overline{P_e} - P_a) \; . \tag{4}$$

This expression is used to evaluate thrust for the mean axial flow model described in Section 4 and is also appropriate for combustion chambers with an ideal exit nozzle.

As pointed out by Schwer and Kailasanath (2011b), as long as the pressure ratio (plenum/exit) is sufficiently large, the detonation propagation is unaffected by the exit conditions as the flow throughout the combustion chamber remains supersonic. This implies that it is possible to only consider the flow at the inlet of the combustion chamber and an alternative control volume construction analogous to that used by Wintenberger et al. (2003) and Endo et al. (2004) for PDEs to develop an approximate analytical model for RDE thrust. This is the basis of the pressure history model of RDE thrust developed in Section 3.

To develop this alternative method of thrust evaluation, consider the control volume of Fig. 2b which encloses the engine but does not cross the exit plane. Instead, the control volume is placed along the walls of the combustion chamber (in the gas) and crosses the inlet plane of the combustor. This is the same type of control volume that is used in the PDE models of Wintenberger et al. (2003) and Endo et al. (2004). This enables the computation of the thrust based on the conditions at the porous thrust surface with a correction for the drag on the walls of the chamber. The balance of forces in the axial (z) direction for this control volume is

$$F_z = \underbrace{\int_{A_c} (P_c - P_{c,1}) \, \mathrm{d}S}_{I} + \underbrace{\int_{A_c} [\rho_c u_{z,c}^2 + (P_{c,1} - P_a)] \, \mathrm{d}S}_{II} \quad \underbrace{- \int_{A_w} \tau_w \, \mathrm{d}S}_{III} \, , \tag{5}$$

where A_c is the area of the frontal surface of the porous injector at the upstream end of the combustor (labeled thrust wall in Fig. 1a) and A_w is the area of the annular walls of the combustor that are subjected to the shear stress τ_w created by the axial flow. The pressure $P_{c,1}$ is the value of the pressure in the reactant layer just upstream of the detonation wave. In order to make quantitative estimates of the thrust using this control volume analysis, we now consider appropriate approximations for each of the terms in (5).

Term I represents the integrated effects of the detonation-generated pressure force on the injector surface at the upstream end of the combustion chamber. We will assume that radial variation of the pressure is small so that the integral can be evaluated by multiplication of the area, $A_c = \pi(R_o^2 - R_i^2) = 2\pi\overline{R}W$, times the average value of the integrand,

$$F_I = A_c(\overline{P}_c - P_{c,1}) \; . \tag{6}$$

This is exactly analogous to the result used to compute impulse $\mathcal{I}$ for a single-cycle of PDE operation using the temporal average of pressure on the thrust surface rather than the spatial average. To compute the integral, we must compute $\overline{P}_c$ using the operating conditions and geometry of the engine.

Term II represents the force associated with the momentum flux of the gas at the inlet to the combustion chamber. Generally, the flow into the combustion chamber is low-speed and the term ρu^2 does not contribute substantially to the thrust although the pressure difference $P_{c,1} - P_a$ acting on the face of the injector may be significantly different than ambient in some cases. The magnitude of term II will depend on the engineering details of the injection system. If we assume uniform flow over the inlet surface, the approximate value of the integral will be

$$F_{II} \approx A_c(P_{c,1} - P_a) + \overline{u}_c\dot{M} \ . \tag{7}$$

If the average density ρ_c ahead of the detonation wave is known instead of the velocity $\overline{u}_c$, then the estimate is

$$\approx A_c(P_{c,1} - P_a) + \frac{\dot{M}^2}{\rho_c A_c} \ . \tag{8}$$

Term III represents friction due to the viscous forces on the side walls due to flow within the combustion chamber. In addition to the assumptions made above, although not explicitly included in the momentum equation, we assume that the combustion chamber is adiabatic, i.e., heat losses to the chamber walls are neglected. The effect of heat loss will be to reduce the mean effective pressure and thrust from the ideal values computed by the present analysis; just as in the PDE case as discussed by Radulescu and Hanson (2005) and Kawane et al. (2011).

The total thrust will be given by the sum of the three terms

$$\mathcal{T} = F_I + F_{II} + F_{III} \ . \tag{9}$$

Using engineering estimates for each of these three terms we observe that the majority of the contribution to the thrust will be term I, with term II being a factor of 5-10 smaller depending on the fuel and engine specifics and term III is at least one to two orders of magnitude smaller than the sum of terms I and II. The present analysis focuses on term I, estimates term II in order to obtain realistic comparisons with computations and measurements of other researchers, and neglects term III.

This analysis also neglects the contribution of the pressure on the base of the engine located at the exit of the combustor. Interaction between the exit plume and the base may result in the average pressure $\overline{P}_b$ on the base being sufficiently different than the atmospheric pressure P_a that there will be a fourth contribution

$$F_{IV} = A_b(\overline{P}_b - P_a) \tag{10}$$

to the thrust. This approach could also be used to account for the presence of a converging or converging-diverging nozzle, or a conical aero-spike attached to the inner portion of the base. In order to calculate the average base pressure or account for a nozzle, a more detailed flow analysis will be required.

3 Pressure History Model

The pressure history model is based on evaluating the thrust associated with the pressure history on the thrust wall due to the propagation of the detonation and expansion flow of the detonation products. In order to find the average pressure on the thrust wall, we need to model the gas dynamics of the flow field created by the rotating detonation. A simplified model is to consider the propagation of the detonation in a layer of height H over a solid surface, setting aside the effect of porosity of the thrust surface and the inflow of reactants that occurs in an RDE. This is equivalent to assuming that the flow ahead of the detonation is parallel to the thrust surface and the detonation wave is normal to the surface.

This model is best analyzed in the X'-Z' frame that is co-moving with the detonation as shown in Fig. 3. In this frame, the flow is steady and consists of a planar detonation in the reactive layer which creates an oblique shock wave in the bounding gas and an expansion wave behind the detonation. The idealized flow is assumed to be self-similar near the triple point where the waves intersect, this region is shown as the detail in Fig. 3. The postshock state 5, and the state 3 following the expansion wave must be in mechanical balance which means that pressure and the flow deflections are continuous across the contact surface: $P_5 = P_3$; $\theta_5 = \theta_3$. There must also be mechanical balance along the contact surface ahead of the triple point: $P_1 = P_4$; $\theta_1 = \theta_4$. The inflow from the plenum will result in θ_1 being nonzero and a tilted detonation wave as shown in Fig. 1b, however this does not change the triple point balance considerations. More significantly, the periodic nature of the flow will result in a nonzero azimuthal flow $\overline{u}_\theta$ upstream of the oblique shock in the stationary (laboratory) reference frame so that $u_4 \neq u_1$ in the co-moving frame where $u_4 = U_{CJ} + \overline{u}_\theta$ and $u_1 = U_{CJ}$. In this situation, the contact surface 1-4 will be a shear layer with a velocity difference of up to 1000 m/s (See Eude et al., 2011, Fig. 5).

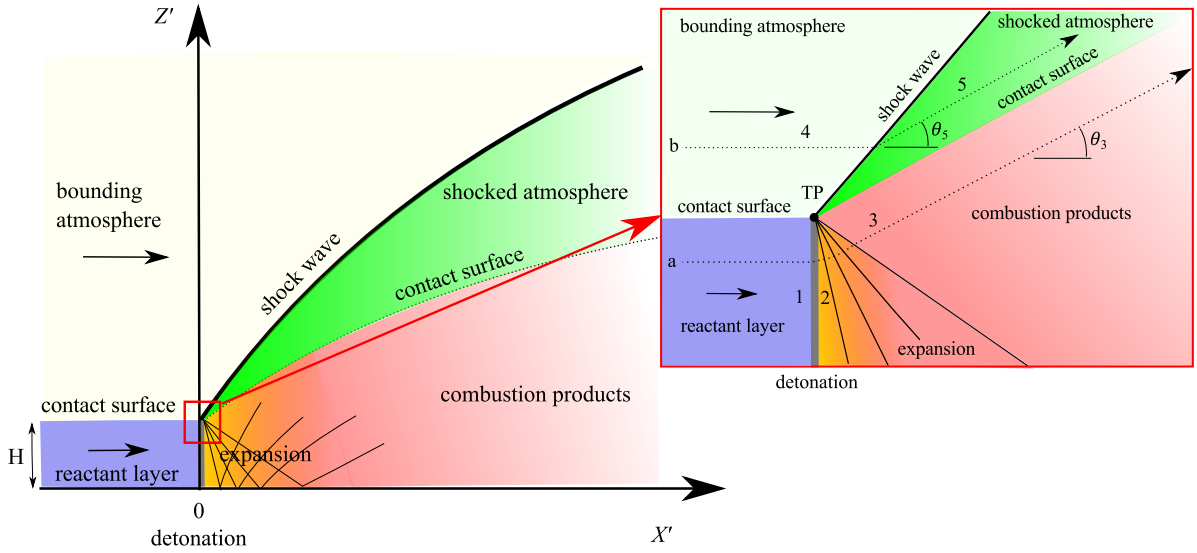

Figure 3: Simplified model for detonation of a uniform layer of thickness H and detail of triple point region (red box).

There are two key issues in applying this model to an RDE. First, a model of the injection process is needed to determine the pressure just upstream of the detonation. Fievisohn and Yu

(2017) discuss a simple control volume model and implementation as boundary condition in their method of characteristics computations. Schwer and Kailasanath (2011a) compare a detailed fluid dynamic model of discrete injectors with two approaches that model injection as a boundary condition. Second, the state of the bounding gas is not known ahead of time but is created by the expansion of the detonation products. In general, this expansion creates a non-uniform state upstream of the shock wave in the bounding gas; this state must be determined in a self-consistent solution considering the periodic flow associated with the annular geometry. Assuming that the pressure upstream of the detonation is given, solutions to the triple-point configuration can be found by assuming isentropic expansion of the detonation products to the upstream pressure in order to define state 4. The iterative solution of the 3-5 contact surface matching problem ($P_3 = P_5$ and $\theta_3 = \theta_5$) is equivalent to graphically finding the intersection of the bounding layer shock polar with the Prandtl-Meyer (PM) expansion solution between states 2 and 3 as shown in Fig. 4 for three cases. There are two possible solutions for states 3 and 5 but the attached oblique shock case that is observed in simulations and experiments is the lower pressure solution located on the supersonic branch of the oblique shock polar. These solutions were computed using realistic thermochemistry and equilibrium properties using the Shock and Detonation Toolbox Browne et al. (2017). The numerical values associated with states 1–5 that were determined by these computations are given in Appendix B for three fuels, hydrogen (H_2), ethylene (C_2H_4) and propane (C_3H_8) with an initial state of $P_1 = 100$ kPa and $T_1 = 300$ K..

Note that all three ideal RDE cases shown in Fig. 4 admit solutions with attached oblique shocks. However, in the most general case of arbitrary conditions in the bounding gas layer, a solution with an attached oblique shock may not exist. This was discussed by Fievisohn and Yu (2017) using ideal gas models of the polars and considering parametric variations of the bounding atmosphere temperature. Our computations with realistic thermochemistry and parameters relevant to RDE operation for a wide range of reactant mixtures give results similar to Fig. 4 and we find that solutions are obtained for states 3 and 5 as long as state 4 corresponds to expanded detonation products. Houim and Fievishon (2017) examined the case of a hot, stationary inert gas atmosphere bounding a cold detonation layer and found that if the bounding layer is sufficiently hot, attached oblique shock solutions are not observed; see Appendix C for further discussion.

The model of Fig. 3 has been examined previously in the context of fuel-air explosions by Sichel and Foster (1979) who considered the impulse delivered by a fuel-air layer bounded by the ground at the bottom and the atmosphere at the top. Sichel and Foster used analytical expressions based on a constant ratio of specific heats (but with different values for shocked air and the combustion products) to determine the solutions for states 5 and 3 for MAPP[2] gas-air and methane-air mixtures over a range of equivalence ratios. The flow field following the detonation was determined using the method of characteristics to compute the interaction of the expansion wave with the ground. The method of Sichel and Foster was recently adapted by Fievisohn and Yu (2017) to the RDE flowfield and extended to include inflow and periodic boundary conditions. Fievisohn and Yu describe their method-of-characteristics solution technique in detail and showed that their solution compared favorably with the finite-difference solution of Schwer and Kailasanath (2011b).

Sichel and Foster (1979) pointed out that if the detonation reaction zone is sufficiently thin, then for purposes of computing impulse from an infinitely long layer, the only relevant dimensional parameters are the layer height H and the detonation overpressure ΔP_{CJ}. Further, it is reasonable

[2]MAPP gas is a mixture of Methyl Acetylene, Propadiene, Propane and other C3 and C4 hydrocarbons

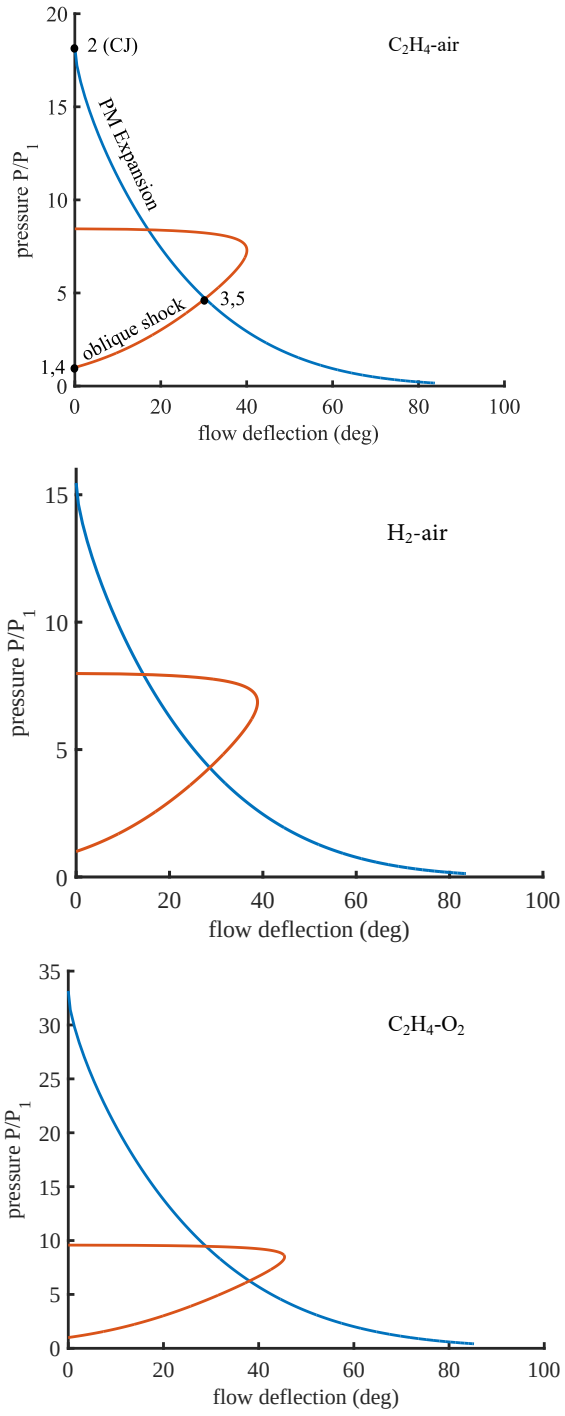

Figure 4: Three examples of pressure-deflection diagrams for 3-5 interface mechanical matching solution.

to suppose that the main features of the flow are governed by inviscid gas dynamics and the conditions behind CJ detonations correspond to sonic flow in wave-fixed coordinates for all mixtures. Considering these factors, they concluded that the pressure along the ground behind the detonation front can then be written in terms of a non-dimensional function ψ and distance $\xi = x/H$ as

$$P(x) - P_{c,1} = (P_{CJ} - P_{c,1})\psi(x/H) = \Delta P_{CJ}\psi(\xi;\gamma_e)\,, \tag{11}$$

where $P_{c,1}$ is the pressure in the layer of explosive gas upstream of the detonation. The function ψ depends on the properties of the combustion products, indicated here as a dependence on the ratio of specific heats γ_e. Using (11) for the distribution of pressure along the thrust surface in an RDE, we evaluate the average pressure (1) due to the detonation in terms of an integral of the nondimensional pressure

$$\overline{P}_c - P_{c,1} = \Delta P_{CJ}\frac{H}{2\pi\overline{R}}\int_0^{2\pi\overline{R}/H}\psi(\xi)\,\mathrm{d}\xi\,. \tag{12}$$

The integral for a given value of $2\pi\overline{R}/H$ and γ_e is a nondimensional function K, defined as

$$K = \int_0^{2\pi\overline{R}/H}\psi(\xi;\gamma_e)\,\mathrm{d}\xi\,. \tag{13}$$

As discussed by Bykovskii et al. (2006), there is another essential scaling function of the height H and the annulus width W. As is well-established from fundamental studies (Lee, 2008) on detonation behavior, the magnitude of H and W relative to the detonation wave cellular structure size (cell width or length) or equivalently reaction zone length, is a key consideration in determining if detonations can be initiated and propagate continuously. If the layer height or annulus width is too small (Bykovskii et al., 2006) relative to the detonation cellular structure width or length, it will be impossible to initiate and sustain continuous detonation. These are very important practical considerations and will determine the range of fuel-oxidizer-diluent compositions as well as injection conditions for successful operation of a given combustor fixture in the continuous detonation mode. In the present analysis we are assuming that these conditions are met and the only role of the layer height is as a gas dynamic scaling parameter.

Sichel and Foster (1979) found the function ψ to be relatively independent of the gas composition so they proposed a universal relationship that could be used to compute the pressure and impulse for a range of fuel-air detonations. The RDE computations by Schwer and Kailasanath (2013) for injection face pressure also support this notion, with consistent pressure distributions for H_2 and a variety of C2 and C3 hydrocarbons in air and distinct but also consistent distributions for the fuel-O_2 cases; two examples are shown in Fig. 5; the lines are data digitized from Fig. 7 and 9 of Schwer and Kailasanath (2013).

Motivated by the success of simple analytic fits to the expansion wave behind propagating detonations (Beltman and Shepherd, 2002), we propose the following model for the pressure decay (along the injection surface) behind the detonation front,

$$\psi(\xi) = \exp(-\alpha\xi)\,, \tag{14}$$

where α is a constant that is determined from fitting the data. Note that this model does not describe the narrow pressure spike and peak at the detonation front that is shown in Fig. 5. This

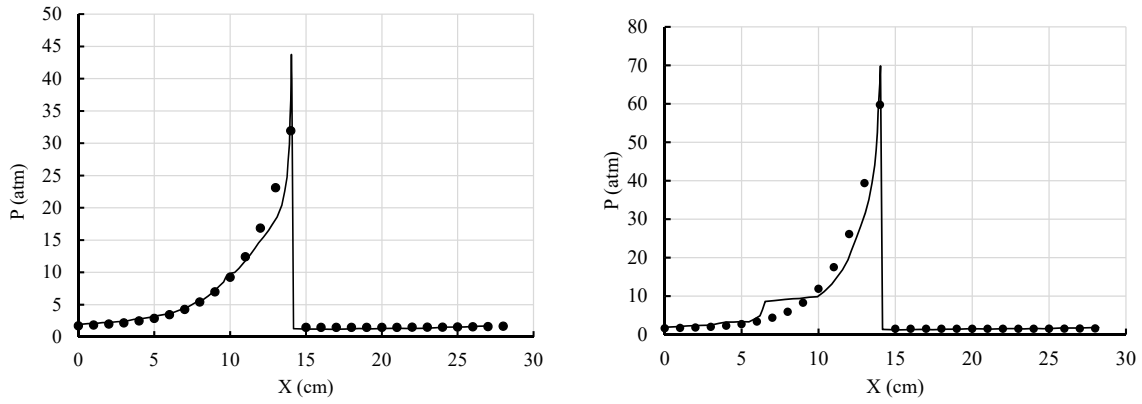

Figure 5: Pressure at injector face (lines) Schwer and Kailasanath (2013) compared to the exponential decay model (points) described in text. a) Stoichiometric C_2H_4-air and b) Stoichiometric C_2H_4-O_2.

spike represents the high pressure behind the leading shock front, decaying rapidly to the CJ pressure with the first cm behind (to the left on this graph) the leading shock front located at 14 cm. This spike contributes a negligible amount to the impulse and as in the previous model of PDE performance, will be neglected. Integration of the normalized pressure signal yields a value of K = 1.02. For comparison, analysis of the results of Sichel and Foster yields K =1.3, the higher value is consistent with the larger confining effect[3] associated with a cold air bounding layer as compared to hot detonation products. Using the parameters given by Schwer and Kailasanath (2013) for a C_2H_4-air detonation with initial conditions of 150 kPa and 255 K, and a layer height of 3.2 cm, we obtain from our model equations, (11) and (14), the points shown in Fig. 5a for a value of $\alpha = 1/K$ = 0.98. Although the model results do not exactly match the pressure profile near the wave front, the results are both qualitatively and quantitatively reasonable.

The layer heights are substantially different for fuel-air and fuel-oxygen cases analyzed by Schwer and Kailasanath (2013); in order to compare the present model with their results it is necessary to use the mass flux and conditions ahead of the detonation to compute H using mass conservation

$$H = \frac{\dot{M}}{\rho_c W U_{CJ}} \ . \tag{15}$$

Using this estimate, the fuel-oxygen cases of Schwer and Kailasanath (2013) were analyzed. Direct integration of the pressure trace shown in Fig. 5b yields K = 1.54; the model pressure history using $\alpha = 1/K = 0.65$ yields the points shown in Fig. 5b. The differences between simulations and model pressure histories are larger than in the C_2H_4-air case due to the presence of a shock wave within the expansion flow; apart from this obvious discrepancy, the model is a reasonable empirical approximation to the simulation results. The difference in α between fuel-air and fuel-oxygen cases can be attributed to the differences in the combustion product properties due the the larger energy content and substantially higher detonation product temperatures in fuel-oxygen mixtures as compared to fuel-air mixtures. As a consequence, flow deflection angles θ_3 are larger for the

[3]The extent of this effect can judged from the difference in values of $\theta_3 \approx 20°$ for Sichel and Foster compared to $\theta_3 \approx 30°$ for the RDE cases (Appendix B) using fuel-air mixtures.

fuel-oxygen cases than for fuel-air cases but the pressures P_3 are also higher. Systematic studies using numerical simulations for a range of mixtures will be needed to further clarify the dependence of K on mixture properties.

The value of K can be obtained by analytic evaluation which can be simplified in most cases because the $2\pi\overline{R}/H$ is between 10–20. This means that the upper limit to the integration in (13) can be taken to be $+\infty$ without any loss in fidelity for the purpose of the present model so that

$$K \approx \int_0^\infty \exp(-\alpha\xi)\, \mathrm{d}\xi = \frac{1}{\alpha} \,. \tag{16}$$

3.1 Evaluating the thrust

From (12) and (13) , the average thrust due to the detonation is

$$F_I = \Delta P_{CJ} \frac{A_c H}{2\pi\overline{R}} K = \Delta P_{CJ} W H K \,, \tag{17}$$

and based on the analysis presented in the previous section, we use $K = 1.02$ for fuel-air mixtures and $K = 1.54$ for fuel-oxygen mixtures. The specific thrust due to the detonation is defined as $F_I/\dot{M}$, where $\dot{M}$ is the total (fuel and oxidizer combined) mass flow rate. The total mass flow rate can either be computed from the inflow velocity, $\dot{M} = A_c \rho_c u_c$ or from the rate of mass consumption by the detonation, $\dot{M} = HW\rho_c U_{CJ}$. Using the second approach, the specific thrust is

$$\frac{F_I}{\dot{M}} = \frac{\Delta P_{CJ}}{\rho_c U_{CJ}} K \,. \tag{18}$$

This expression can be further simplified by using the following approximate expression (Browne et al., 2017) for ideal gas CJ pressure,

$$\Delta P_{CJ} \approx \frac{\rho_c U_{CJ}^2}{\gamma_e + 1} \,. \tag{19}$$

Substituting this expression into (18), we obtain

$$\frac{F_I}{\dot{M}} \approx K \frac{U_{CJ}}{\gamma_e + 1} \,. \tag{20}$$

Another typical figure of merit for RDEs and PDEs is the specific impulse per unit mass of fuel consumed divided by the acceleration of earth's gravity g . Defining the fuel mass fraction as $Y_f = \dot{M}_{fuel}/\dot{M}$, the specific impulse per unit mass of fuel consumed in one revolution of the detonation is

$$I_{spf,I} = \frac{F_I}{Y_f g \dot{M}} \,, \tag{21}$$

which can be approximated as

$$I_{spf,I} \approx \frac{K}{Y_f g} \frac{U_{CJ}}{\gamma_e + 1} \,. \tag{22}$$

Values of specific thrust and the fuel-based specific impulse due to detonation alone for a range of equivalence ratios and either air or pure oxygen as the oxidizer are shown in Fig. 6 for three

representative fuels. These computations are based on computed CJ properties with the state just upstream of the detonation at 295 K and 100 kPa; however, we expect that these specific performance measures will be relatively independent of conditions upstream of the detonation. This is based on the functional form of (20) and (22) and the known modest dependence of U_{CJ} and γ_e on initial conditions.

The variations in specific thrust with equivalence ratio shown in Fig. 6a are a consequence of the dependence of the CJ speed on the energy content of the mixture and the sound speed of mixture upstream of the detonation. This is discussed at length in Wintenberger et al. (2003) and a consequence of the thermodynamic relations that determine the CJ state as discussed in Appendix B of Browne et al. (2017). The trends with equivalence ratio shown in Fig. 6b are primarily due to the inverse dependence on fuel mass fraction of the model (21) and are the same trends that are predicted by the PDE model of Wintenberger et al. (2003). The fuel-based specific impulse of C_2H_4 and C_3H_8 are indistinguishable throughout the equivalence ratio range because the energy content per unit mass of these fuels as well as other alkanes is essentially identical.

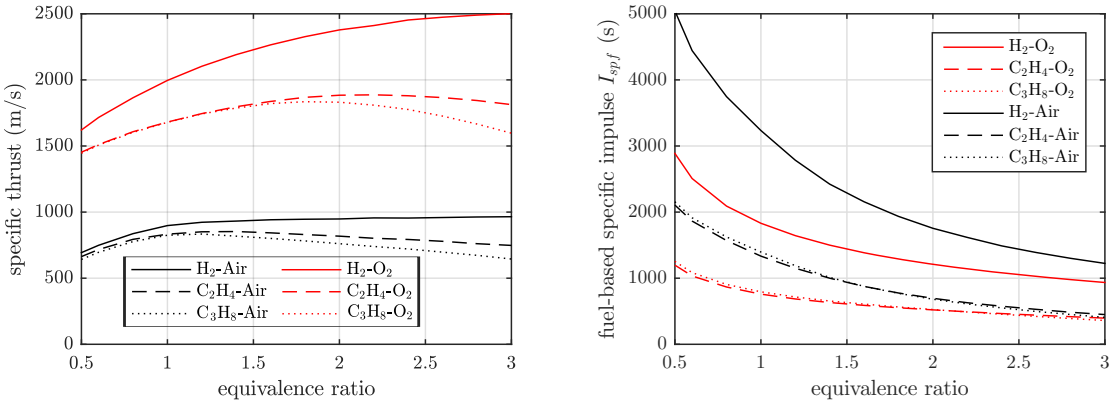

(a) (b)

Figure 6: a) Specific thrust $\mathcal{T}/\dot{M}$ and b) fuel-based specific impulse I_{spf} of RDEs as predicted using the pressure history model.

So far, we have considered a single detonation wave but multiple waves are often observed (Kato et al., 2016; George et al., 2017). Consider a number N of waves within the chamber, all rotating in the same direction (counter-rotating waves introduce additional complications that we have not considered). For a total mass flow rate $\dot{M}$ through the combustor, each wave combusts mass at the rate

$$\dot{M}_i = \dot{M}/N \ . \tag{23}$$

The height H_i of each wave will be given by mass conservation

$$H_i = \frac{\dot{M}_i}{\rho_c W U_{CJ}} = H/N \ , \tag{24}$$

where H is the height of a single wave at the same mass flow rate. The nondimensional integral of the pressure has an upper bound of

$$\frac{(2\pi/N)\overline{R}}{H/N} = \frac{2\pi\overline{R}}{H} \tag{25}$$

which is independent of N because the extent of the "tail" of the pressure wave behind detonation wave will be $1/N$ of the total circumference of the combustion chamber. This implies that the ideal value of the nondimensional integral is independent of the number of waves

$$K_i = K = \int_0^{2\pi\overline{R}/H} \exp(-\alpha\xi)\, \mathrm{d}\xi \tag{26}$$

or in dimensional terms

$$K = \frac{1}{\Delta P_{CJ} H} \int_0^{2\pi\overline{R}} \left(P_c(x) - P_{c,1}\right)\, \mathrm{d}x \tag{27}$$

and if there are N waves each of height H_i, the effective height of the equivalent single wave is given by

$$H = N H_i \ . \tag{28}$$

The net thrust associated with the detonation pressure on the combustor inlet from all N waves will be the sum of the thrust of each individual wave

$$F_I = \sum_{i=1}^{N} \Delta P_{CJ} W H_i K_i \tag{29}$$

$$= \sum_{i=1}^{N} \Delta P_{CJ} W \frac{H}{N} K \tag{30}$$

$$= \Delta P_{CJ} W \frac{H}{N} K \sum_{i=1}^{N} 1 \tag{31}$$

$$= \Delta P_{CJ} W H K \ , \tag{32}$$

which is identical to the result obtained for a single wave. This is a consequence of the scaling of all spatial dimensions with the height of the detonation wave. The insensitivity of the thrust to the number of detonation waves is confirmed by numerical simulations (Yi et al., 2011; Tsuboi et al., 2017).

4 Axial Flow Model

Although the detonation wave rotates, this does not result in a net (average) azimuthal rotational flow at the exit of the combustion chamber if, as is usually the case, the flow entering the chamber does not have a net azimuthal rotation. This does not mean that the velocity in the azimuthal direction vanishes everywhere within the flow field, but at any axial location z, there are positive and negative values of azimuthal velocity which average out so that the total angular momentum is zero.

To show this, consider the angular momentum about the z-axis of the coordinate system shown in Fig. 7. The angular momentum of an element of volume $\mathrm{d}V$ is

$$\boldsymbol{r} \times \rho \boldsymbol{u}\, \mathrm{d}V \ . \tag{33}$$

The conservation of angular momentum for a stationary control volume Ω with control surface $\partial\Omega$ is

$$\boldsymbol{M} = \frac{\partial}{\partial t}\int_{\Omega} \boldsymbol{r} \times \rho \boldsymbol{u}\, \mathrm{d}V + \int_{\partial\Omega} (\boldsymbol{r} \times \rho \boldsymbol{u})\, \boldsymbol{n} \cdot \boldsymbol{u}\, \mathrm{d}S\,, \tag{34}$$

where M is the total torque exerted on the control volume. For an annular control volume that encompasses the RDE shown in Fig. 7, the imposed net torque is zero as the engine is not rotating, there are no rotating components within the flow path and we are neglecting the effect of friction on the combustion chamber walls. Because the flow is periodic, averaging over one period of the cycle will result in the first term on the right-hand side averaging to zero, leaving

$$0 = \frac{1}{T}\int_0^T \int_{\partial\Omega} (\boldsymbol{r} \times \rho \boldsymbol{u})\, \boldsymbol{n} \cdot \boldsymbol{u}\, \mathrm{d}S\, \mathrm{d}t\,. \tag{35}$$

For the geometry of Fig. 7, the integral can be written in terms of velocity components and simplified by transforming to the wave-fixed (steady flow) frame of reference

$$0 = \int_A R\rho u_\theta u_z\, \mathrm{d}S\,, \tag{36}$$

where R is the perpendicular distance from the point in the flow to the z axis and A is the area of the annulus perpendicular to the z axis, the direction of the mean axial flow. If we further suppose that the flow is uniform in the radial direction, this reduces to

$$\frac{1}{2\pi}\int_0^{2\pi} \rho(\theta', z) u_\theta(\theta', z) u_z(\theta', z)\, \mathrm{d}\theta' = \overline{\rho u_\theta u_z} = 0\,. \tag{37}$$

Axial and azimuthal velocities are correlated as shown by Fig. 5 of Schwer and Kailasanath (2011b) with fluctuations of u_z about a mean positive value and both positive and negative excursions of u_θ that support the notion that (37) will be satisfied. The fluctuations in velocity and density are the consequence of the flow field, particularly the oblique shock waves, which simulations show decay in strength with distance from the detonation layer. This suggests that sufficiently far from the detonation layer the flow will primarily be axial and relatively uniform in the azimuthal direction. Using the nomenclature of Appendix A, $u_\theta = v$ and $u_z = w$, the vanishing of the mean angular momentum suggests that the mean azimuthal flow speed will be small in comparison to the mean axial flow speed

$$\overline{v} \ll \overline{w} \tag{38}$$

far downstream from the detonation layer. The validity of this assumption will depend on the axial length of the combustor and represents an idealization, one that is important in formulating the axial flow model presented in this section.

4.1 Modeling the expansion process

The net result of the two-dimensional expansion process within the annular combustion chamber is to convert the flow from the almost entirely azimuthal flow immediately following the detonation to primarily axial flow at the chamber exit. The expansion simultaneously decelerates the flow induced by the detonation and turns the azimuthal flow of the detonation products so that it becomes

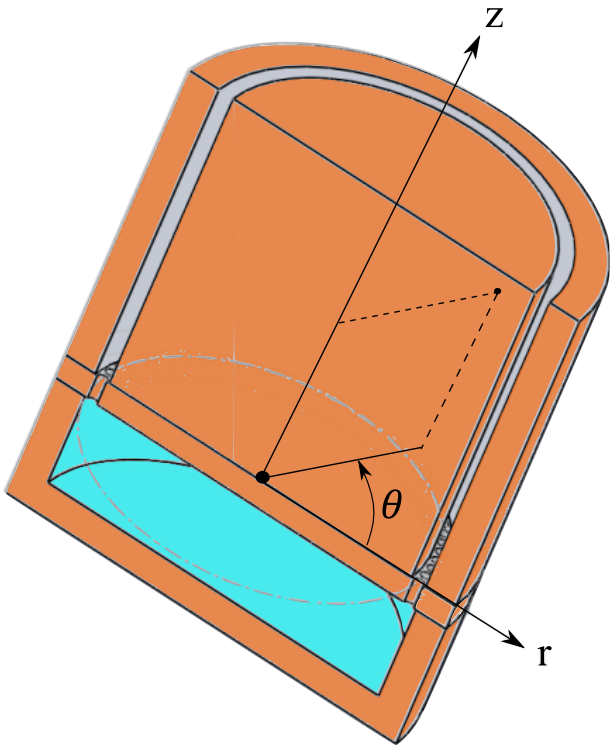

Figure 7: Geometry of rotating detonation combustion chamber and associated axisymmetric coordinate system.

predominantly axial. Interaction of the flow with the oblique shock wave results in further reduction of the azimuthal flow components. We anticipate that if the combustion chamber is sufficiently long, then the azimuthal flow can be neglected, and the performance upper bound can be based on the same notions as traditional rocket motor performance based on quasi-one-dimensional flow. The extent to which the flow approaches a purely axial state will depend on the length of the combustor compared to the height of the detonation layer. Examples of the diminished azimuthal flow at the exit of the combustor can be found in the simulations of Yi et al. (2011); Schwer and Kailasanath (2011b); Davidenko et al. (2007).

The basis of ideal steady-flow analyses in propulsion systems with shock and detonation waves is the conservation of total enthalpy (Wintenberger and Shepherd, 2006) along streamlines. In the wave-fixed (steady flow) frame in the unwrapped 2-D coordinates, this is expressed as (see Appendix A)

$$h_t = h + \frac{1}{2}(u'^2 + w'^2) \tag{39}$$

which in the laboratory (unsteady flow) frame for a detonation rotating with azimuthal speed U_D transforms to

$$h_1 = h + \frac{1}{2}(v^2 + w^2) - vU_D \ . \tag{40}$$

Considering a fixed axial location, the velocity and enthalpy will be a function of time or equivalently azimuthal location. Using the averaging technique of (1), the average of (40) can be written

$$\overline{w^2} = 2(h_1 - \overline{h}) - \overline{v^2} + 2\overline{v}U_D \ . \tag{41}$$

As discussed in the previous section, the conservation of angular momentum (37) indicates that if the axial flow is sufficiently uniform, then the average azimuthal speed at the end of the combustor will be negligible, $\overline{v} \approx 0$. However, simulations demonstrate that fluctuations in v are not necessarily negligible, i.e., $\overline{v^2} > 0$, at the end of annular combustors with dimensions commonly used in testing. The effect of fluctuations in v on the r.m.s. value of axial flow speed w at the exit can be estimated from (41)

$$\sqrt{\overline{w^2}} = \sqrt{2(h_1 - \overline{h}) - \overline{v^2}} = \sqrt{2(h_1 - \overline{h})}\left[1 - \frac{\overline{v^2}}{2(h_1 - \overline{h})}\right]^{1/2} , \tag{42}$$

by assuming $\overline{v} = 0$. Numerical evaluation of (42) reveals that if the r.m.s. average of the azimuthal speed, $\sqrt{\overline{v^2}}$, is 30% of the ideal axial speed, $\sqrt{2(h_1 - \overline{h})}$, this will result in an approximately 5% fluctuation (r.m.s.) in the axial velocity contribution to the average specific thrust. Given this modest effect on the thrust we will neglect the effect of azimuthal and axial speed fluctuations, taking the effective axial speed at the exit to be the ideal value computed from the mean thermodynamic state at the engine exit

$$\overline{w} \approx \sqrt{2(h_1 - \overline{h})} \ . \tag{43}$$

The enthalpy can be considered a function of composition, pressure P and entropy s. In an expansion wave following a detonation, the flow time scales are sufficiently long compared to the chemical time scales (see Wintenberger et al. 2004) that the flow is to a reasonable approximation in chemical equilibrium and so that $h = h(P, s)$ only. In the ideal version of the flow that we are considering, entropy changes are due only to the flow crossing shock waves. However, the shock waves are relatively weak, resulting in a modest loss in total pressure, for example about 7% in the simulations by Yi et al. (2011). As a consequence we can consider the axial velocity to be a function of pressure only and the entropy is taken to be constant and equal to the value of the CJ state; for this ideal model we assume that detonation propagates at the CJ speed, $U_D = U_{CJ}$. With these assumptions we obtain the following simple expression for the axial flow velocity, which appears identical in form to the expression used in ideal quasi-one-dimensional flow models:

$$w = \sqrt{2(h_1 - h(P, s_2))} \, , \tag{44}$$

with the important distinction that $h(P, s_2)$ is the enthalpy on the isentrope associated with the two-dimensional flow created by the products of the rotating detonation. The result (44) and the underlying assumptions have been used by previous researchers, particularly by Davidenko et al. (2011), who carried out both multi-dimensional numerical simulations and modeling of an ideal RDE based on axial exit flow. Davidenko et al. (2011) carried out an extensive parametric study for H_2-O_2 mixtures comparing an ideal conventional rocket engine with ideal RDE performance based on the axial flow approximation. Using axial flow models for RDE analysis has a long history and some elements of the present model can be found in the pioneering studies by the University of

Michigan group (Shen and Adamson, 1972; Adamson and Olsson, 1967; Nicholls et al., 1966) on the RDE configurations of the type shown in Fig. 1.

The enthalpy $h(P, s_2)$ of the combustion products downstream of the detonation as a function of pressure is shown in Fig. 8. At the CJ state (2), the conservation of total enthalpy across the detonation wave implies $h_2 = h_1 + \frac{1}{2}(U_{CJ}^2 - w_2^2)$ and there are no solutions (the dashed portion of the curve) to (44) for $P_{CJ} \geq P \geq P_m$, where the limiting pressure P_m is defined by $h(P_m, s_2) = h_1$. In the case shown in Fig. 8a, the limiting pressure ratio $P_m/P_1 = 4.18$ ($P_1 = 100$ kPa) and axial flow solutions for $P_m > P > P^*$ are subsonic and for $P^* > P$ are supersonic. The limiting pressure P_m corresponds to the effective one-dimensional (axial flow) stagnation pressure since the axial flow speed is zero at this point. Computations for a wide range of compositions indicates that $P_m \approx$ 0.22-0.25 P_2.

For given values of the exit pressure P and ambient pressure P_a, the specific thrust can be estimated by (45) as a function of exit pressure assuming uniform axial flow and the control volume of Fig. 2a.

$$\frac{\mathcal{T}}{\dot{M}} = w + \frac{P - P_a}{\rho w} \ . \tag{45}$$

The density ρ and axial speed w are computed assuming isentropic expansion from the CJ state and (44) so that the right-hand side is only a function of pressure. An example of specific thrust for $P_a = 100$ kPa is shown in Fig. 8b as a function of exit pressure. Excluding the sharp changes as $P \rightarrow P_m$ or 0, the results are insensitive to pressure over a wide range of values. This suggests that a single value of specific thrust can be estimated from the axial model without specifying the precise value of the exit pressure. The model is valid not only for constant-area combustors but also for combustors with variable area; for example, those with attached ideal nozzles which can be treated as quasi-one-dimensional flow.

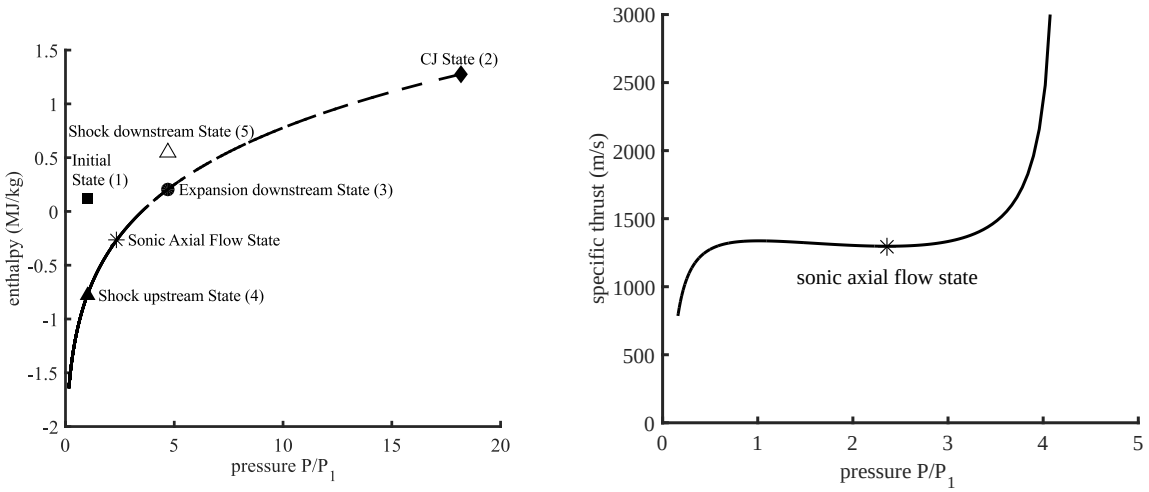

(a) (b)

Figure 8: Axial flow RDE model for C_2H_4-air: a) Pressure-enthalpy states; b) Specific thrust.

Using the value of specific impulse predicted at the sonic point, the results for three fuels are shown in Fig. 9. The results are remarkably similar to those obtained using the detonation pressure history method shown in Fig. 6. The quantitative values for specific thrust and impulse predicted

by the axial flow model can be up to 30% higher than for the pressure history model for fuel-air cases but there is less than 10% difference for the fuel-oxygen cases. The values of the specific thrust computed with the axial flow model depend not only on the composition of the reactants but also the thermodynamic conditions in the reactants just ahead of the detonation. Parametric computations for the case of C_2H_4-Air mixtures are shown in Fig. 10.

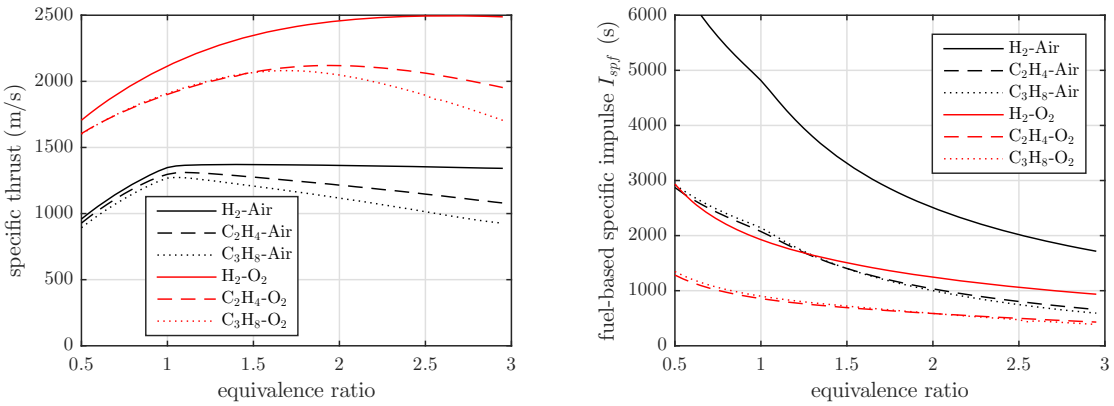

(a) (b)

Figure 9: Sonic axial flow RDE model: a) Specific thrust $\mathcal{T}/\dot{M}$; b) fuel-based specific impulse I_{spf}.

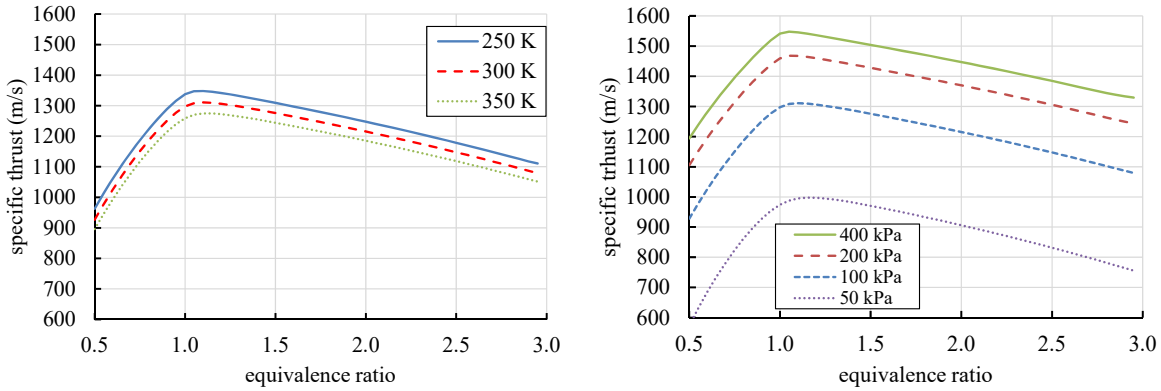

(a) (b)

Figure 10: Sonic axial flow RDE model: a) Effect of initial temperature T_1 for P_1 = 100 kPa; b) Effect of initial pressure P_1 for T_1 = 300 K.

4.2 Analytical Expressions

The one-γ analytical model of the CJ state can be used with perfect gas thermodynamic expressions to estimate the specific thrust. The starting point is the expression (Browne et al., 2017) for CJ

Mach number in terms of energy release per unit mass

$$M_{CJ} - \frac{1}{M_{CJ}} = \sqrt{\frac{2q(\gamma^2 - 1)}{\gamma R T_1}} \ . \tag{46}$$

The CJ temperature and pressure are

$$T_{CJ} = T_1 \frac{(\gamma M_{CJ}^2 + 1)^2}{M_{CJ}^2(\gamma + 1)^2} \tag{47}$$

and

$$P_{CJ} = P_1 \frac{\gamma M_{CJ}^2 + 1}{(\gamma + 1)} \ . \tag{48}$$

The enthalpy of the reactants is

$$h_1 = C_P T_1 + q \tag{49}$$

and the enthalpy of the products is

$$h = C_P T \ . \tag{50}$$

The product temperature can be computed from the change in pressure and entropy along the streamline emanating from state 2 (CJ)

$$T = T_2 \exp\left(\frac{s - s_2}{C_p}\right)\left(\frac{P}{P_2}\right)^{R/C_p} \ . \tag{51}$$

The change in entropy can be estimated from the change in total pressure along the streamline assuming the total temperature remains constant

$$s - s_2 = -R \ln\left(\frac{P_t}{P_{t,2}}\right) \ . \tag{52}$$

These expressions can be used to derive an explicit expression for specific thrust for the particular case of exit pressure equal to the atmospheric pressure ($P = P_a$). As shown in Fig. 9, the specific thrust is relatively insensitive to the exit pressure so we choose the pressure-matched condition to make the computation of specific thrust particularly simple. Assuming[4] isentropic expansion along the streamlines, $s = s_2$, we obtain

$$\left.\frac{\mathcal{T}}{\dot{M}}\right|_{P_a} = w = \sqrt{2C_p T_1}\left[1 + \frac{q}{C_P T_1} - \left(\frac{P_a}{P_1}\right)^{(\gamma-1)/\gamma}\left(\frac{P_1}{P_2}\right)^{(\gamma-1)/\gamma}\frac{T_2}{T_1}\right]^{1/2} \ . \tag{53}$$

[4]Evaluating the entropy change for a total pressure loss of 7% results in correction to (51) of less than 1% to the isentropic temperature.

Substituting the analytical expressions for $T_2 = T_{CJ}$ and $P_2 = P_{CJ}$, we obtain an explicit expression

$$\left.\frac{\mathcal{T}}{\dot{M}}\right|_{P_a} = a_1\sqrt{\frac{2}{\gamma-1}}\left[1+\frac{1}{2(\gamma+1)}\left(M_{CJ}-\frac{1}{M_{CJ}}\right)^2-\left(\frac{P_a}{P_1}\right)^{(\gamma-1)/\gamma}\frac{1}{M_{CJ}^2}\left(\frac{\gamma+1}{\gamma M_{CJ}^2+1}\right)^{-(\gamma+1)/\gamma}\right]^{1/2}. \tag{54}$$

For the range $5 < M_{CJ} < 8$ and $1.1 < \gamma < 1.15$ which are of interest for RDEs, numerical evaluation gives reasonable agreement (within 10%) to the value computed using detailed thermochemistry for $P_1 = P_a$. Examining the range of values for M_{CJ} for fixed γ, the specific thrust is observed to be linearly proportional to CJ velocity, just as in the RDE analysis and consistent with the pressure history model. We conclude that the scaling relationship

$$\frac{\mathcal{T}}{\dot{M}} \propto U_{CJ} \tag{55}$$

is a feature of both PDE (64) and RDE (20) models; this result could be anticipated from dimensional analysis although there are a number of ways in which a characteristic velocity could be defined. For example, (54) can be interpreted as an example of a relationship of the form

$$\frac{\mathcal{T}}{\dot{M}} = a_1 f(M_{CJ}, \gamma, P_a/P_1) \tag{56}$$

as the consequence of dimensional analysis and without further examination of the functional form of f, it is not obvious that (55) holds.

Expression (54) is useful in discussing the dependence of specific thrust on temperature and pressure that is shown in Fig. 10. The modest increase in specific thrust with a decrease in initial temperature (Fig. 10a) is due to the dependence of M_{CJ} on T_1 as given by (46). The more dramatic increase in specific thrust with increasing P_1 for a given P_a is due to the decrease in enthalpy with decreasing pressure; the CJ temperature (T_2/T_1) and pressure ratios (P_2/P_1) are essentially independent of initial pressure so that a decrease in enthalpy and the corresponding increase in specific thrust is entirely due to the greater isentropic expansion resulting from smaller pressure ratios, $P_a/P_2 = P_a/P_1 \cdot P_1/P_2$.

4.3 Axial Flow Model and Nozzles

Sufficiently far downstream from the detonation where the axial flow approximation is valid, the usual quasi-one dimensional flow methodology employed for ideal rocket motor performance estimates (Sutton, 1992, Chap. 3) can be used to examine the effect of a nozzle on the performance of a RDE. Relationship (44) is identical to the conservation of energy relation for a nonreacting quasi-one dimensional flow if we recognize that the effective total temperature T_t is defined by $h_1 = C_pT_1 + q = C_pT_t$ and $h = C_PT$. This is equivalent to defining the total temperature as the constant pressure combustion temperature as suggested by Kato et al. (2016). The constant pressure combustion temperature has a modest dependence on pressure so that a single value of T_t can be used for a given mixture composition and a wide range of combustor pressures. The conservation of energy (44) applies along a streamline in the flow and is equally valid within the constant area combustor and an attached nozzle. As a consequence, the results of the axial flow model and the specific thrust estimates (45) apply to configurations with nozzles downstream of the combustor

and as examined below, the usual ideal rocket motor analysis can be applied using the appropriate stagnation conditions.

To relate the axial flow model to the usual perfect gas methodology, the axial speed relation

$$w = \sqrt{2(h_1 - h(P, s_2))} \tag{57}$$

can be approximated using the perfect gas model as

$$w \approx \sqrt{2(C_P T_t - C_p T)} = \sqrt{\frac{2\gamma R T_t}{\gamma - 1}} \left(1 - \frac{T}{T_t}\right)^{1/2} \tag{58}$$

for $T \leq T_t$ ($P \leq P_t$). The standard perfect gas isentropic relationships can be used to define temperature and density in terms of pressure. The density, axial speed and flow area A are related through the conservation of mass flow.

$$\dot{M} = \rho w A \ . \tag{59}$$

These relationships can be used to evaluate the specific thrust for a given nozzle exit area A using (4). For a given mass flow rate, an effective sonic throat area A^* can be defined based on the sonic point in the expansion. At the sonic point $w* = a*$, the mass flow will be

$$\dot{M}^* = \rho^* a^* A^* = \rho_t a_t \frac{\rho^*}{\rho_t} \frac{a^*}{a_t} A^* \ . \tag{60}$$

Apply the perfect gas thermodynamic relationships, we obtain the standard relationship for mass flow through a choked nozzle in terms of the stagnation conditions

$$\dot{M}^* = A^* P_t \left[\frac{\gamma}{R T_t} \left(\frac{2}{\gamma + 1} \right)^{\gamma + 1/\gamma - 1} \right]^{1/2} \ . \tag{61}$$

Consider the situation in which the mass flow rate through the combustor is determined by the injector system and a nozzle is attached to the end of the combustor. For a given total temperature T_t, the chamber stagnation pressure P_t will be determined by the constancy of mass flow for steady operation and the value of the nozzle throat area (Kato et al., 2016).

$$P_t = \frac{\dot{M}}{A^*} \left[\frac{R T_t}{\gamma} \left(\frac{\gamma + 1}{2} \right)^{\gamma + 1/\gamma - 1} \right]^{1/2} \ . \tag{62}$$

As the nozzle area decreases, the stagnation pressure increases as observed in the tests of Kato et al. (2016). The axial flow model computations show that $P_t \propto P_2 = C \cdot P_2/P_1 \cdot P_1$ where $C \approx 0.24$ so that increases in P_t will result in proportional increases in P_1 because P_2/P_1 is nominally a constant for a given mixture. Likewise, for fixed values of A^*, the pressure P_t or P_1 will increase proportional to increases in mass flow rate as observed in the tests of Kato et al. (2016).

5 Comparisons with simulations

The simulation parameters for four cases are given in Table 1 together with a comparison of simulation results to model estimates for the fuel-based specific impulse. The specific impulse values estimated by the present models are within 5-10% of the values computed by Schwer and Kailasanath (2013); the fuel-air estimates are slightly higher than the Schwer and Kailasanath (2013) values; the fuel-oxygen values are slightly lower except for the C_2H_4-O_2 axial flow model. Term II amounts to 20% of the thrust for the H_2-air case and 15% for the C_3H_8-O_2 case. The pressure history model results shown in Table 1 were made using (7) and the value of $\overline{u}_c$ = 300 m/s given by Schwer and Kailasanath (2013). The axial flow model results used the same pressure and temperature (1.5 atm and 255 K) ahead of the detonation as the pressure history model. The PDE model results are consistently lower (by up to 11%) than the axial sonic flow model results but comparable to both the pressure history model predictions and the simulation values.

Table 1: Parameters for the cases reported in Schwer and Kailasanath (2013) and comparison of numerical simulations with models of fuel-based specific impulse.

case	H_2-air	C_2H_4-air	C_2H_4-O_2	C_3H_8-O_2
Model Input and CJ Parameters				
$\dot{M}$ (kg/s)	0.950	1.12	1.91	0.884
ρ_c (kg/m^3)	1.48	2.04	2.19	2.41
H (mm)	32.4	29.9	15.1	15.4
α	0.98	0.98	0.65	0.65
U_{CJ} (m/s)	1982	1836	2402	2383
P_{CJ} (MPa)	2.75	3.24	5.97	6.46
γ_e	1.169	1.165	1.142	1.137
Y_f	0.02852	0.06375	0.2260	0.2160
Fuel-Based Specific Impulse				
Unsteady 2D simulations, Schwer and Kailasanath (2013)				
I_{spf} S&K (s)	4860	1990	700	1070
Pressure History Model				
$I_{spf}(I+II)$ (s)	4706	1975	704	1016
Axial Flow Model				
I_{spf} (s)	5383	2280	911	952
PDE Model, Wintenberger et al. (2003)				
I_{spf} (s)	4761	1985	750	781

6 Comparison to Test Results

Kato et al. (2014, 2016) performed experiments using a C_2H_4-O_2 fueled RDE to directly measure the average thrust with a load cell and instrumented the plenum and combustion chamber with pressure transducers. The annular RDE chamber had an inner radius of 30.25 mm, an outer radius

of 33.45 mm and was approximately 100 mm long. The fuel and oxygen were injected from separate plenums using impingement to promote mixing with the fuel injection being axial and the oxygen injection oriented radially outward. The plenum pressures were approximately 5 to 10 times the average combustion chamber pressure. The flow through the injectors was choked and mass flow rates were measured by using an electronic scale to determine the change in mass of the supply tanks. The thrust was measured over an operational period of 0.2 to 0.8 s depending on the mass flow rate and equivalence ratio.

Comparisons between measured specific thrust (assumed to be the load cell output) and model predictions for selected tests from Kato et al. (2016) are shown in Fig. 11 using both the pressure history and axial sonic flow models. Analyses of these tests require making assumptions about the state of the reactants just upstream of the detonation front as there are no time-resolved measurements available for the pressure or temperature. The measured values of mass flow rate and static pressure in the downstream portion of the combustor were used to compute the total pressure at that point assuming axial flow as discussed in Kato et al. (2016). The pressure just ahead of the detonation is inferred by using the observation from the axial flow model results that the total pressure is approximately 0.24 times the Chapman-Jouguet pressure and performing an inverse CJ computation to determine P_1 corresponding to $P_{CJ} = P_t/0.24$. The static temperature was assumed to be equal to the value in the plenum. Some tests in Kato et al. (2016) used a convergent or converging-diverging nozzle so that strictly speaking, the pressure history model is not applicable and should only be compared to those tests with just the constant area combustion channel.

Experimental values of specific thrust are 20-60% less than the pressure history estimates as shown in Fig. 11a, which may indicate a highly non-ideal detonation process with significant losses, resulting in speeds much less than the CJ value. The influence of mixing on detonation propagation is discussed by Fujii et al. (2017) and Gaillard et al. (2015) who describe the challenges obtaining uniform mixtures with impinging jets. The filled data in Fig. 11a are for combustors with a constant area and the open data points are for cases with nozzles. The data in Fig. 11b are for both constant as well as variable area cases. Representative ranges of values for the pressure P_1 inferred from the experimental conditions are 35 to 40 kPa for the low mass flow cases and 60 to 70 kPa for the high mass flow model. The test data trends in Fig. 11b are consistent with sonic axial flow model for the high-mass-flow cases but show significant deviations for the fuel-rich, low-mass-flow cases. Just as in the pressure history model, the test data are lower than the axial sonic flow model prediction values in all cases. A key source of uncertainty that may be responsible for the differences between model predictions and measurements is the lack of experimental data for the pressure and temperature of the reactant gas layer just upstream of the detonation. Other possible causes for the differences between model predictions and test data include nonideal mixing and detonation processes as well as deviations from ideal axial flow at the exit of the test fixture. Resolving these issues will require further tests and analyses.

7 Comparison of RDE and PDE analysis

The RDE performance model can be compared with the PDE model of Wintenberger et al. (2003) if we recognize that PDE impulse per cycle is the analog of RDE thrust and PDE mass per cycle is the analog of RDE mass flow rate. PDE specific impulse I/M is therefore the analog of RDE

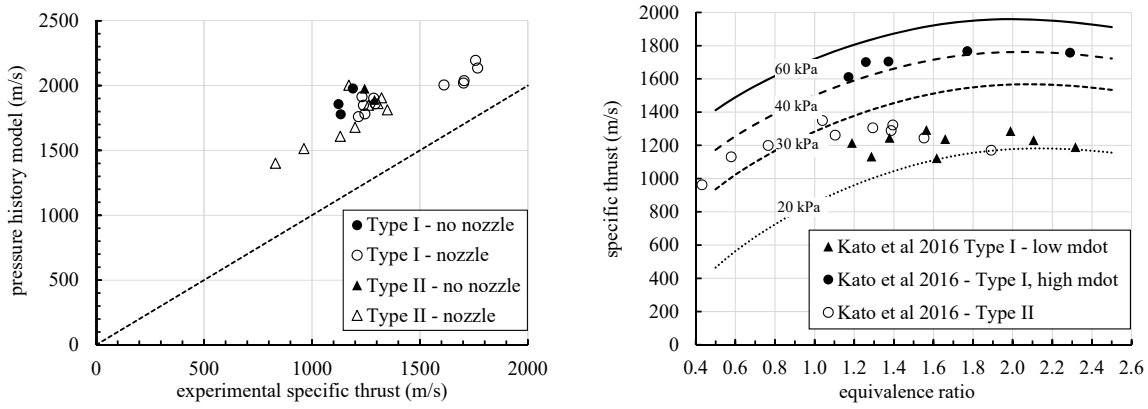

(a) (b)

Figure 11: a) Measured and model estimates of specific thrust $\mathcal{T}/\dot{M}$ for the C_2H_4-O_2 RDE tests of Kato et al. (2016). (a) Pressure history model and (b) sonic axial flow model; lines are predictions, points are test data.

specific thrust $\mathcal{T}/\dot{M}$ and PDE fuel-based specific impulse $I_{spf} = I/(gY_fM)$ is the analog of RDE fuel-based specific impulse $I_{spf} = \mathcal{T}/(gY_f\dot{M})$. Specific thrust and specific impulse not only have the same units for both PDEs and RDEs but the analytical models have exactly the same dependence on the detonation thermodynamic parameters. From equation (27) of Wintenberger et al. (2003), the analytical model for impulse per PDE cycle is

$$I_{PDE} = K_{PDE}V\frac{\Delta P_3}{U_{CJ}} \,. \tag{63}$$

To compare this to the RDE impulse, the plateau pressure difference ΔP_3 can be expressed in terms of the CJ pressure, $\Delta P_3 \approx 0.35\Delta P_{CJ}$, and we use the nominal value of $K_{PDE} = 4.3$ given by Wintenberger et al. (2003). The mass of gas that participates in each cycle of the detonation process is $M = \rho_c V$. Substituting these relations into (63), we obtain the following expression for the PDE analog of specific thrust due to the detonation

$$\left(\frac{I}{M}\right)_{PDE} \approx 1.5\frac{\Delta P_{CJ}}{\rho_c U_{CJ}} \,, \tag{64}$$

which is identical in form to the RDE pressure-history specific thrust expression (18) but with a constant $K = 1.5$ in place of $K_{RDE} = 1.02$–1.54 (fuel-air vs. fuel-oxygen). This is the reason for the surprisingly good qualitative correlation (Fig. 12) of measured RDE performance with the PDE model, as originally observed by Rankin et al. (2017). As shown in Fig. 12, the pressure history and sonic axial flow RDE models bound the data for both RDE and PDE tests. The systematic discrepancy between the RDE pressure history model and the RDE data can be explained by noting that only term I of the model could be estimated from the information available in Rankin et al. (2017). The sonic axial flow model appears to be about 10% higher than the experimental data for H_2-air cases and less than 5% higher for the C_2H_4-air cases.

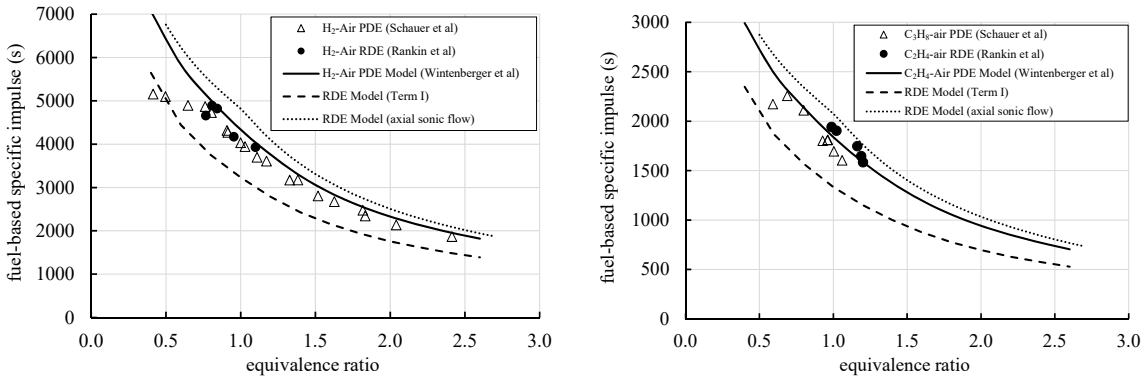

(a) (b)

Figure 12: Comparison of predicted RDE and PDE performance with measured performance using data from Fig. 10 of Rankin et al. (2017). a) H_2-air. b) C_2H_4-air.

8 Conclusion

The analyses given in this paper provide simple mechanistic explanations and relationships to predict RDE performance using either elementary thermochemical computations or approximate analytical models based on perfect gas relationships. The analyses also demonstrate why RDE and PDE models give very similar trends and identical qualitative dependence on detonation properties. The pressure history model indicates how quantitative differences in performance occur due to the differences in the pressure-time history at the thrust surface and the possible importance of the thrust associated with the filling process in the RDE case. The axial flow model provides a way to account for both pressure and mass flow contributions to thrust without explicitly evaluating the contributions to the integrals required for the pressure history model. Both the pressure history and axial flow models require knowledge of the conditions just upstream of the detonation; reinforcing the importance of the fuel-oxidizer injection and mixing processes to the performance of RDEs. The axial flow model provides a simple upper bound on the effective stagnation conditions which can be used in the traditional quasi-one dimensional rocket motor methodology to estimate performance of RDEs used in a rocket motor configuration.

Acknowledgment

The authors thank the Japan Society for the Promotion of Science for an Invitation Fellowship for Research that supported a visit to Nagoya University in the fall of 2015.

References

T. C. Adamson, Jr. and G. R. Olsson. Performance Analysis of a Rotating Detonation Wave Rocket Engine. *Astronautica Acta*, 13:405–415, 1967.

W. M. Beltman and J. E. Shepherd. Linear Elastic Response of Tubes to Internal Detonation Loading. *Journal of Sound and Vibration*, 252(4):617–655, 2002. doi: 10.1006/jsvi.2001.4039.

S. Browne, J. Zeigler, and J. E. Shepherd. Numerical Solution Methods for Shock and Detonation Jump Conditions. GALCIT FM2006-R3, California Institute of Technology, Pasadena, CA, January 2017. URL http://shepherd.caltech.edu/EDL/publications/reprints/ShockDetonation.pdf.

F. A. Bykovskii, S. A. Zhdan, and E. G. Vedernikov. Continuous Spin Detonations. *Journal of Propulsion and Power*, 22(6):1204–1216, 2006. doi: 10.2514/1.17656.

D. M. Davidenko, I. Gokalp, and A. N. Kudryavstev. Numerical Simulation of the Continuous Rotating Hydrogen-Oxygen Detonation with a Detailed Chemical Mechanism. In *West-East High Speed Flow Field Conference*, Moscow, Russia, November 2007.

D. M. Davidenko, Y. Eude, I. Golkap, and F. Falempin. Theoretical and Numerical Studies on Continuous Detonation Wave Engines. In *17th AIAA International Space Planes and Hypersonic Systems and Technologies Conference*, San Francisco, California, April 2011. doi: 10.2514/6.2011-2334.

T. Endo, J. Kasahara, A. Matsuo, K. Inaba, S. Sato, and T. Fujiwara. Pressure History at the Thrust Wall of a Simplified Pulse Detonation Engine. *AIAA Journal*, 42(9):1921–1930, 2004. doi: 10.2514/1.976.

Y. Eude, D. M. Davidenko, I. Gokalp, and F. Falempin. Use of the Adaptive Mesh Refinement for 3d Simulations of a CDWRE (Continuous Detonation Wave Rocket Engine). In *17th AIAA International Space Planes and Hypersonic Systems and Technologies Conference*, San Francisco, California, April 2011. doi: 10.2514/6.2011-2236.

R. T. Fievisohn and K. H. Yu. Steady-State Analysis of Rotating Detonation Flowfields with the Method of Characteristics. *Journal of Propulsion and Power*, 33(1):89–99, 2017. doi: 10.2514/1.B36103.

M. L. Fotia, J. L. Hoke, and F. R. Schauer. Experimental Performance Scaling of Rotating Detonation Engines Operated on Gaseous Fuels. *Journal of Propulsion and Power*, 33(5): 1187–1196, 2017. doi: 10.2514/1.B36213.

J. Fujii, Y. Kumazawa, A. Matsuo, S. Nakagami, K. Matsuoka, and J. Kasahara. Numerical Investigation on Detonation Velocity in Rotating Detonation Engine Chamber. *Proceedings of the Combustion Institute*, 36:2665–2672, 2017. doi: 10.1016/j.proci.2016.06.155.

T. Gaillard, D. Davidenko, and F. Dupoirieux. Numerical Optimisation in Non Reacting Conditions of the Injector Geometry for a Continuous Detonation Wave Rocket Engine. *Acta Astronautica*, 111:334–344, 2015. doi: 10.1016/j.actaastro.2015.02.006.

A. St. George, R. Driscoll, V. Anand, and E. Gutmark. On the Existence and Multiplicity of Rotating Detonations. *Proceedings of the Combustion Institute*, 36:2691–2698, 2017. doi: 10.1016/j.proci.2016.06.132.

R. W. Houim and R. T. Fievishon. The Influence of Acoustic Impedance on Gaseous Layered Detonations Bounded by an Inert Gas. *Combustion and Flame*, 179:185–198, 2017. doi: 10.1016/j.combustflame.2017.02.001.

K. Ishihara, Y. Kato, K. Matsuoka, J. Kasahara, A. Matsuo, and I. Funaki. Performance Evaluation of Rotating Detonation Engine with Conical-Shape Tail. In *53rd AIAA Aerospace Sciences Conference*, Kissimmee, Florida, January 2015. doi: 10.2514/6.2015-0630.

K. Kailasanath. Recent Developments in the Research on Rotating-Detonation-Wave Engines. In *55th AIAA Aerospace Sciences Conference*, Grapevine, TX, January 2017. doi: 10.2514/6.2017-0784.

Y. Kato, K. Ishihara, K. Gawahara, K. Matsuoka, J. Kasahara, A. Matsuo, and I. Funaki. Thrust Measurement of Rotating Detonation Engine by Sled Test. In *50th AIAA/ASME/SAE/ASEE Joint Propulsion Conference*, Cleveland, OH, July 2014. doi: 10.2514/6.2014-4034.

Y. Kato, K. Ishihara, K. Matsuoka, J. Kasahara, A. Matsuo, and I. Funaki. Study of Combustion Chamber Characteristic Length in Rotating Detonation Engine with Convergent-Divergent Nozzle. In *54th AIAA Aerospace Sciences Conference*, San Diego, CA, January 2016. doi: 10.2514/6.2016-1406.

K. Kawane, S. Shimada, J. Kasahara, and A. Matsuo. The Influence of Heat Transfer and Friction on the Impulse of a Detonation Tube. *Combustion and Flame*, 158:2023–2036, 2011. doi: 10.1016/j.combustflame.2011.02.017.

J. H. S. Lee. *The Detonation Phenomenon*. Cambridge University Press, New York, NY USA, 2008.

F. A. Lyman. On the Conservation of Rothalpy in Turbomachines. *Journal of Turbomachinery*, 115:521–526, July 1993. doi: 10.1115/1.2929282.

J. A. Nicholls, R. E. Cullen, and K. W. Ragland. Feasibility Studies of a Rotating Detonation Wave Rocket Motor. *Journal of Spacecraft and Rockets*, 3(6):893–898, 1966. doi: 10.2514/3.28557.

M. I. Radulescu and R. K. Hanson. Effect of Heat Loss on Pulse-Detonation-Engine Flow Fields and Performance. *Journal of Propulsion and Power*, 21(2):274–285, 2005. doi: 10.2514/1.10286.

B. A. Rankin, M. L. Fotia, A. G. Naples, C. A. Stevens, J. L. Hoke, T. A. Kaemming, S. W. Theuerkauf, and F. R. Schauer. Overview of Performance, Application, and Analysis of Rotating Detonation Engine Technologies. *Journal of Propulsion and Power*, 33(1):131–143, January 2017. doi: 10.2514/1.B36303.

D. Schwer and K. Kailasanath. Effect of Inlet on Fill Region and Performance of Rotating Detonation Engines. In *47th AIAA/ASME/SAE/ASEE Joint Propulsion Conference and Exhibit*, San Diego, CA, 2011a. doi: 10.2514/6.2011-6044.

D. Schwer and K. Kailasanath. Numerical Investigation of the Physics of Rotating-Detonation-Engines. *Proceedings of the Combustion Institute*, 33:2195–2302, 2011b. doi: 10.1016/j.proci.2010.07.050.

D. Schwer and K. Kailasanath. Fluid Dynamics of Rotating-Detonation-Engines with Hydrogen and Hydrocarbon Fuels. *Proceedings of the Combustion Institute*, 34:1991–1998, 2013. doi: 10.1016/j.proci.2012.05.046.

P. I-W Shen and T.C. Adamson, Jr. Theoretical Analysis of a Rotating Two-Phase Detonation in Liquid Rocket Motors. *Astonautica Acta*, 17(4-5):715–728, 1972. ISSN 0004-6205.

M. Sichel and J. C. Foster. The Ground Impulse Generated by a Plane Fuel-Air Explosion with Side Relief. *Acta Astronautica*, 6(3-4):243–256, 1979. doi: 10.1016/0094-5765(79)90096-1.

G. P. Smith, D. M. Golden, M. Frenklach, M. W. Moriarty, B. Eiteneer, M. Goldenberg, C. T. Bowman, R. K. Hanson, S. Song, W. C. Gardiner, V. V. Lissianski, and Z. Qin. GRI-Mech, July 1999. URL http://www.me.berkeley.edu/gri_mech/.

G. P. Sutton. *Rocket Propulsion Elements*. Wiley, New York, NY USA, 6th edition, 1992.

N. Tsuboi, E. Seiichiro, A. K. Hayashi, and T. Kojima. Front Cellular Structure and Thrust Performance on Hydrogen-Oxygen Rotating Detonation Engine. *Journal of Propulsion and Power*, 33(1):100–111, 2017. doi: 10.2514/1.B36095.

E. Wintenberger and J. E. Shepherd. The Stagnation Hugoniot Analysis for Steady Combustion Waves in Propulsion Systems. *Journal of Propulsion and Power*, 22(4):835–844, 2006. doi: 10.2514/1.12779.

E. Wintenberger, J. M. Austin, M. Cooper, S. Jackson, and J. E. Shepherd. An Analytical Model for the Impulse of a Single-Cycle Pulse Detonation Tube. *Journal of Propulsion and Power*, 19 (1):22–38, 2003. doi: 10.2514/2.6099.

E. Wintenberger, M. Cooper, F. Pintgen, and J. E. Shepherd. Reply to Comment on "Analytical Model for the Impulse of Single-Cycle Pulse Detonation Tube" by M. I. Radulescu and R. K. Hanson. *Journal of Propulsion and Power*, 20(5):957–959, 2004. doi: 10.2514/1.9441.

T.-H. Yi, J. Lou, C. Turangan, J.-Y. Choi, and P. Wolanski. Propulsive Performance of a Continuously Rotating Detonation Engine. *Journal of Propulsion and Power*, 27(1):171–181, 2011. doi: 10.2514/1.46686.

R. Zhou, D. Wu, and J.-P. Wang. Progress of Continuously Rotating Detonation Engines. *Chinese Journal of Aeronautics*, 29(1):15–29, 2016. doi: 10.1016/j.cja.2015.12.006.

A Equations of Motion

The equations of motion for inviscid compressible flow can be written as:

$$\frac{\partial \rho}{\partial t} + \boldsymbol{\nabla} \cdot (\rho \boldsymbol{u}) = 0 \; ; \tag{65}$$

$$\rho \frac{\partial \boldsymbol{u}}{\partial t} + \rho(\boldsymbol{u} \cdot \boldsymbol{\nabla})\boldsymbol{u} = -\boldsymbol{\nabla} P \; ; \tag{66}$$

$$\rho \frac{\partial}{\partial t}\left(h + \frac{1}{2}|\boldsymbol{u}|^2\right) + \rho(\boldsymbol{u} \cdot \boldsymbol{\nabla})\left(h + \frac{1}{2}|\boldsymbol{u}|^2\right) = -\frac{\partial P}{\partial t} \; . \tag{67}$$

In terms of the components of velocity (u, v, w) and the cylindrical coordinate system (r, θ, z) shown in Fig. 7, these equations are:

$$\frac{\partial \rho}{\partial t} + \frac{\partial}{\partial r}(\rho u) + \frac{1}{r}\frac{\partial}{\partial \theta}(r \rho v) + \frac{\partial}{\partial z}(\rho w) = 0 \; ; \tag{68}$$

$$\frac{\partial u}{\partial t} + u\frac{\partial u}{\partial r} + \frac{v}{r}\frac{\partial u}{\partial \theta} + w\frac{\partial u}{\partial z} - \frac{v^2}{r} = -\frac{1}{\rho}\frac{\partial P}{\partial r} \; ; \tag{69}$$

$$\frac{\partial v}{\partial t} + u\frac{\partial v}{\partial r} + \frac{v}{r}\frac{\partial v}{\partial \theta} + w\frac{\partial w}{\partial z} + \frac{uv}{r} = -\frac{1}{\rho r}\frac{\partial P}{\partial \theta} \; ; \tag{70}$$

$$\frac{\partial w}{\partial t} + u\frac{\partial w}{\partial r} + \frac{v}{r}\frac{\partial w}{\partial \theta} + w\frac{\partial w}{\partial z} = -\frac{1}{\rho}\frac{\partial P}{\partial z} \; ; \tag{71}$$

$$\frac{\partial}{\partial t}\left(h + \frac{1}{2}|\boldsymbol{u}|^2\right) + \left(u\frac{\partial}{\partial r} + \frac{v}{r}\frac{\partial}{\partial \theta} + w\frac{\partial}{\partial z}\right)\left(h + \frac{1}{2}|\boldsymbol{u}|^2\right) = -\frac{1}{\rho}\frac{\partial P}{\partial t} \; . \tag{72}$$

The relation to the 2D, "unwrapped" coordinate is through the approximations of neglecting motion in the r direction by setting $u = 0$ and taking $\partial/\partial r = 0$. This results in an inconsistency for the radial momentum which reduces in the limit $u = 0$ to

$$\frac{v^2}{r} = \frac{1}{\rho}\frac{\partial P}{\partial r} \tag{73}$$

and because v does not vanish, there must be a radial pressure gradient. However, if the radius of the annulus R is sufficiently large, the pressure gradient in the radial direction will be small in comparison to the azimuthal and axial gradients and can be neglected. Formally this can be accomplished by taking the limit $r \to \infty$ in the 3D equation set.

To transform to wave-fixed coordinates in 2D, define the following coordinate and velocity transformations using the mean radius $\overline{R}$ of the combustion chamber.

$$x' = U_D t - \overline{R}\theta \; ; \tag{74}$$

$$z' = z \; ; \tag{75}$$

$$t' = t \; ; \tag{76}$$

and

$$u' = U_D - v \; ; \tag{77}$$

$$w' = w \; . \tag{78}$$

This transformation corresponds to going from the laboratory frame (θ-Z) representation in Fig. 1b to the unwrapped wave-fixed frame (X'-Z')in Fig. 3. The velocity components in the unwrapped frame are (u', w') corresponding to the coordinates (x', z'). The detonation is located at $x' = 0$ and the thrust surface is located at $z' = 0$ in the transformed variables. The quantities ρ, P and h are invariant, i.e., the same in both coordinate systems. The equations of motion transform exactly to the 2D steady-flow compressible (Euler) equations in this limit:

$$\frac{\partial}{\partial x'}(\rho u') + \frac{\partial}{\partial z'}(\rho w') = 0 \; ; \tag{79}$$

$$u'\frac{\partial u'}{\partial x'} + w'\frac{\partial u'}{\partial z'} = -\frac{1}{\rho}\frac{\partial P}{\partial x'} \; ; \tag{80}$$

$$u'\frac{\partial w'}{\partial x'} + w'\frac{\partial w'}{\partial z'} = -\frac{1}{\rho}\frac{\partial P}{\partial z'} \; ; \tag{81}$$

$$\left(u'\frac{\partial}{\partial x'} + w'\frac{\partial}{\partial z'}\right)\left[h + \frac{1}{2}(u'^2 + w'^2)\right] = 0 \; . \tag{82}$$

One implication of the energy equation is that the total enthalpy is constant along streamlines in the wave-fixed frame,

$$h_t = h + \frac{1}{2}(u'^2 + w'^2) = \text{constant} \; . \tag{83}$$

In this frame of reference, the flow is steady and total enthalpy is conserved across both shock and detonation waves enabling evaluation of the total enthalpy at any convenient point along a streamline. In the flow just ahead of the detonation $h = h_1$, $w' = 0$ and $u' = U_D$ so that

$$h_t = h_1 + \frac{1}{2}U_D^2 \; . \tag{84}$$

If the flow ahead of the detonation has uniform properties, then this is the unique value of stagnation enthalpy for the entire flow field. Transforming (83) to the laboratory reference frame using (77), the total enthalpy is

$$h_t = h + \frac{1}{2}(v^2 + w^2 + U_D^2) - vU_D = \text{constant} \; . \tag{85}$$

Subsituting for the value of h_t from (84) we obtain the alternative expression for total enthalpy conservation, which is used for the axial flow model discussed in Section 4,

$$h_1 = h + \frac{1}{2}(v^2 + w^2) - vU_D \; . \tag{86}$$

In the limit as the azimuthal velocity vanishes, $v \longrightarrow 0$, the axial flow velocity is given by

$$w|_{axial} = \sqrt{2(h_1 - h)} \; . \tag{87}$$

Although at first glance this appears to be inconsistent with the same limit for (83), in the co-rotating frame, conservation of angular momentum requires that $u' \rightarrow U_D$ in the limit of purely axial flow in the laboratory frame. Substituting (84) in (83), we find that

$$h_1 = h + \frac{1}{2}(w'^2 + u'^2 - U_D^2)\,, \tag{88}$$

which gives a result identical to (87) in the limit of purely axial flow, recognizing that $w' = w$.

In the context of turbomachinery, the expression on the right-hand side of (86) is referred to as the *rothalpy* and U_D is tangential speed of the rotor. A detailed discussion of this concept is given by Lyman (1993).

B Solutions to Triple-Point Configuration

The pressure-deflection states shown in Fig. 4 were computed using equilibrium thermochemistry to determine the detonation state, oblique shock state and Prandtl-Meyer expansion with the methods described in Browne et al. (2017). Selected numerical values associated with each state are given in Table 2. Initial conditions for all cases are stoichiometric mixtures with $P_1 = 0.1$ MPa and $T_1 = 300$ K; velocities are all given in the wave-fixed frame. State 4 was determined by isentropic expansion of the detonation state 2 to the initial pressure P_1 assuming one-dimensional flow parallel to the x axis. The solutions for states 3 and 5 were determined by numerical solution of the pressure and deflection matching conditions at the 3-5 contact surface. The reported values of enthalpy are mixture averages including the heats of formation for each species with the concentrations determined by the equilibrium solutions. The 53 species found in GRI-Mech 3.0 (Smith et al., 1999) were used for these computations with the thermodynamic data fits corrected for discontinuities and the temperature range extended to 6000 K.

Table 2: Triple-point and axial-flow solution states for representative fuel-air and fuel-oxygen mixtures.

		H_2-air	C_2H_4-air	H_2-O_2	C_2H_4-O_2	C_3H_8-O_2
State 1 - Initial Conditions						
ρ_1	(kg/m^3)	0.838	1.15	0.482	1.24	1.36
h_1	(kJ/kg)	2.61	122.	4.47	425	-506.
u_1 (U_{CJ})	(m/s)	1968	1823	2836	2373	2356
a_1	(m/s)	409	346	539	328	308
State 2 - CJ						
T_2	(K)	2943	2923	3675	3930	3822
P_2	(MPa)	1.55	1.82	1.86	3.31	3.59
ρ_2	(kg/m^3)	1.51	2.09	0.884	2.30	2.53
h_2	(MJ/kg)	1.34	1.28	2.83	2.42	1.46
a_2	(m/s)	1091	1005	1542	1281	1269
γ		1.163	1.161	1.129	1.139	1.134
State 3 - PM Expansion						
T_3	(K)	2479	2455	3288	3423	3324
P_3	(MPa)	0.429	0.470	0.461	0.626	0.653
ρ_3	(kg/m^3)	0.506	0.655	0.255	0.526	0.557
h_3	(MJ/kg)	0.145	0.204	0.104	0.234	-0.736
θ_3	(deg)	28.6	30.3	32.5	38.1	39.0
u_3	(m/s)	1895	1777	2800	2451	2452
a_3	(m/s)	1002	918	1422	1156	1145
State 4 - Upstream of Oblique Shock						
T_4	(K)	1948	1922	2935	2993	2898
ρ_4	(kg/m^3)	0.151	0.180	0.0646	0.101	0.103
h_4	(MJ/kg)	-0.952	-0.780	-2.45	-1.75	-2.74
u_4	(m/s)	2405	2264	3598	3160	3164
a_4	(m/s)	902	825	1310	1045	1036
State 5 - Downstream of Oblique Shock						
T_5	(K)	2602	2593	3346	3528	3439
ρ_5	(kg/m^3)	0.480	0.616	0.245	0.489	0.515
h_5	(MJ/kg)	0.479	0.548	1.07	1.38	0.482
u_5	(m/s)	1710	1572	2429	1929	1891
a_5	(m/s)	1024	942	1451	1200	1193
Axial Sonic Flow						
w^*	(m/s)	951	877	1376	1130	1123
P^*	(MPa)	0.203	0.236	0.253	0.426	0.460
$\mathcal{T}/\dot{M}$	(m/s)	1347	1297	2117	1901	1908

C Existence of Attached Oblique Solutions

Houim and Fievishon (2017) call attention to the role of acoustic impedance ratio Z across the interface between the detonation layer and inert bounding gas, using two-dimensional unsteady simulations with a single-step model of detonation. They define the acoustic impedance ratio Z in terms of the ratio of the impedance ρa of the reactants to that of the bounding gas layer, both evaluated upstream of the wave complex. Using the notation of Fig. 3, this is

$$Z_{14} = \frac{(\rho a)_4}{(\rho a)_1} \ . \tag{89}$$

For constant property model used in Houim and Fievishon (2017), this reduces to $Z = \sqrt{T_1/T_4}$ and values of Z = 1.73, 1, 0.71, 0.55 and 0.29 were used in their simulations (corresponding to T_4 = 100, 300, 600, 1000 and 3500 K for T_1 = 298 K. They found that in all cases except for T_4 = 3500 K, a solution was obtained with an attached oblique shock wave, corresponding to the configurations shown in Fig. 4. For case 5 (T_4 = 3500 K) of Houim and Fievishon (2017), the solution consisted of a detached precursor shock (oriented normal to the interface and propagating in the inert bounding layer) followed by an oblique shock in the cold reactant layer that intersects a nominally normal detonation wave in the reactant layer. A secondary oblique shock is needed to match the conditions associated with the PM expansion within the detonation products. Although these cases generally still result in an expansion wave following the detonation, the scaled variation of pressure with distance along the thrust surface may be significantly different for detached and attached oblique shock solution. Solutions of this type (normal precursor shock in the inert bounding layer) will be unsteady because the flow behind the detached normal shock is subsonic relative to the shock wave, resulting in acoustic feedback coupling the precursor shock propagation with the flow downstream of the triple point. This is in contrast to the attached oblique shock cases discussed in Section 3; these all have supersonic flow behind the oblique shock and disturbances generated by the flow downstream of the triple point do not propagate upstream.

Simulations by Houim and Fievishon (2017) raise the interesting possibility that more complex flowfields may result than shown in Fig. 1 or 3. Analyses of triple-point configuration for cases similar to those examined by Houim and Fievishon (2017) are shown in Fig. 13. In Fig. 13a, all cases except for 3500 K (comparable to Case 5 of Houim and Fievishon (2017)) display an intersection between the oblique shock polar and PM expansion behind the detonation. These cases admit a mean flow solution with an attached oblique shock, which is consistent with the unsteady simulations of Houim and Fievishon (2017). The polars do not intersect for the 3500 K case, consistent with the detached shock solution observed in their unsteady simulations.

There are several key differences between the simulations of Houim and Fievishon (2017) and the RDE situation. One key difference is that the expanded detonation products are moving relative to the reactant layer, resulting in shear flow between the inert gas layer and reactants. Parametric computations with four layer speeds are shown in Fig. 13 for detonation of a stoichiometric C_2H_4-O_2 layer (T_1 = 300 K, P_1 = 1 atm) bounded by a layer of air at various initial temperatures and velocities. These solutions show that attached oblique shock solutions are possible if the bounding gas speed is sufficiently high; the speed of the flow of the bounding inert gas layer is given relative to the reactant layer in the direction opposed to the detonation motion in the laboratory frame. The velocity required to obtain attached shock solutions are comparable to those of state 4 in the model RDE cases we have examined, see Table 2. Other significant factors include the bounding gas layer

temperature, which is much lower for fuel-air than fuel-oxygen cases, and significant differences in the value of γ, the ratio of specific heats compared to what was used in the Houim and Fievishon (2017) simulations. The consequences of these differences is that for RDEs, attached oblique shock solutions such as shown in Fig. 4 appear to be possible in all the cases we have examined.

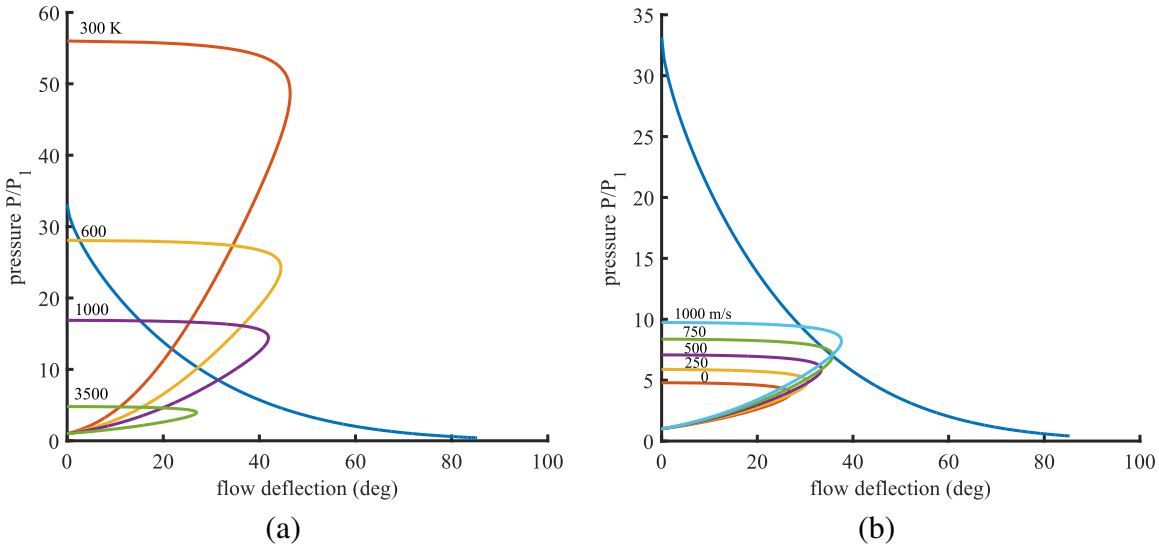

Figure 13: Pressure-flow deflection analyses. (a) Effect of air temperature (b) Effect of shear flow for 3500 K air temperature.

All other factors being equal, the existence of attached shock solutions can be correlated with the ratio Z_{14} but is it clear from examining the behavior of the shock polars in Fig. 13 that this is caused by decrease in the inert layer Mach number with increasing sound speed for fixed U_1 and T_1, resulting in the shift of the shock polar relative to the PM expansion. An even larger shift in the relative location of the PM and oblique shock polar occurs due to the change in the reactant composition from fuel-oxygen to fuel-air, as shown in Fig. 4. In general, the existence of attached shock solutions will depend on M_1, γ_1, M_4 and γ_4 (using one-γ approximations for each layer) and is not correlated with Z_{14} alone.

Houim and Fievishon (2017) unsteady simulations indicate that transmission of the transverse waves across the boundary between detonation products (state 3) and shocked inert gas (state 5) does appear to be a significant factor is determining if detonations will successfully propagate within the reactant layer. If we treat the interactions of the transverse waves with the 3–5 interface in the acoustic limit, then the ratio

$$Z_{35} = \frac{(\rho a)_5}{(\rho a)_3} \tag{90}$$

will be relevant to the contact surface interaction of transverse waves associated with detonation instability rather than Z_{14}. From Table 2, values of Z_{35} are 1; whereas the values for the contact surface upstream of the detonation Z_{14} are between 0.25 and 0.40. This difference between upstream and downstream values of Z can explain the confinement of transverse waves to the detonation layer in case 5 of Houim and Fievishon (2017) and stability of detonation propagation despite the lack of a stable attached oblique shock solution.